International Journal of Non-Linear Mechanics 125 (2020) 103539

Contents lists available at ScienceDirect

International Journal of Non-Linear Mechanics

journal homepage: www.elsevier.com/locate/nlm

Prediction of elastic moduli and ultimate strength of fiber/yarn-reinforced elastic–plastic matrix using Fourier series approach and cuboidal/wedge sub-volumes

G. Gopinath [a], R.C. Batra [b,*]

[a] Wethersfield, CT 06109, USA

[b] Department of Biomedical Engineering and Mechanics, M/C 0219, Virginia Polytechnic Institute and State University, Blacksburg, VA 24061, USA

ARTICLE INFO

Keywords:
Micromechanics
Homogenization
Fourier series analysis
Fiber shape
Plain/twill weave
Elastic–plastic matrix

ABSTRACT

Homogenization of mechanical properties of a heterogeneous material using analytical/semi-analytical micromechanics approaches is computationally less expensive than that through numerical techniques. However, analytical methods cannot be easily applied to a complex distribution of the microstructure in a unit cell (or a representative volume element). Here, we alleviate this by accommodating cuboidal and wedge shaped sub-volumes in the Fourier series approach (FSA). This is akin to using penta- and hexa-hedral elements to discretize the geometry in 3-dimensional finite element analysis (FEA). The technique is applied to study the elasto-plastic response of unidirectional fiber/yarn-reinforced composites with square, circular and star shaped fibers to transverse loading. It is shown that (i) predicted transverse elastic modulus and the shear moduli are sensitive to the fiber shape and the unit cell configuration, (ii) the stress–strain curves for the homogenized composite agree with those reported in the literature found by using the FEA, and (iii) the presently computed elastic constants for plain and 2/2 twill weave fabrics are close to those found by other methods and deduced from the test data. A linear softening model based on plasticity approach is implemented within the FSA to predict failure and progressive softening in the yarn and the resin. It captures the nonlinear response and provides the ultimate strength under tensile loading.

1. Introduction

With advances made in manufacturing and materials sciences, modern composite materials with complex microstructures such as textile fabrics, braids, and inclusions with tailored cross-sections have been developed for applications in automotive, military and aerospace industries. Analytical/semi-analytical micro-mechanics schemes like the Mori–Tanaka (M–T) [1,2], the method of cells (MoCs) [3,4], and the Fourier series approach (FSA) [5,6] provide a general framework for efficiently homogenizing mechanical properties of heterogeneous materials. Analytical approaches are computationally less expensive than the numerical schemes, and hence are more amenable to analyzing large heterogeneous structures using the finite element method (FEM). However, they cannot easily handle complex distributions and geometries of the microstructure.

The M–T scheme provides explicit expressions for stiffness when inclusions are ellipsoidal. However, the method generally fails when either the volume fraction of inclusions is high or inclusions of different shapes are included in an RVE. The MoCs approach is flexible as it involves dividing an RVE into many sub-volumes thereby explicitly allowing for interactions amongst inclusions and considering different RVEs. The method, however, uses only cuboidal sub-volumes that do not easily accommodate inclusions of complex geometries. Fig. 1 depicts how a circular cross-section is often divided into several square/rectangular cells to fill the circular domain. Thus accurately capturing a curved geometry may require numerous sub-cells; e.g., see [7,8] for inclusions of circular and ellipsoidal cross sections. Bednarcyk and Arnold [9] as well as Bednarcyk and Pindera [10] employed the MoCs to analyze plain weave fabrics. Bednarcyk and Arnold [9] found that elastic constants predicted for fabrics were significantly lower than those reported in the literature. They considered a two-step homogenization process to improve upon the estimates. The Fourier Series Analysis (FSA) has generally been restricted to inclusions of simple cross-sections [11–14].

We note that the semi-analytical methods can readily accommodate in-elastic response of its constituents; e.g see Tandon and Weng [15] and Lagoudas et al. [16] for the M–T method; Paley and Aboudi [17] and Ye et al. [7] for the MoCs; and Pruchnicki [18] and Walker et al. [19] for the FSA.

Besides above-mentioned methods, other approaches have been specifically developed to analyze woven fabrics. Ishikawa and Chou [20,21], Naik and Ganesh [22] and Scida et al. [23] have used a laminate

* Corresponding author.
E-mail address: rbatra@vt.edu (R.C. Batra).

https://doi.org/10.1016/j.ijnonlinmec.2020.103539
Received 14 March 2020; Received in revised form 23 June 2020; Accepted 23 June 2020
Available online 26 June 2020

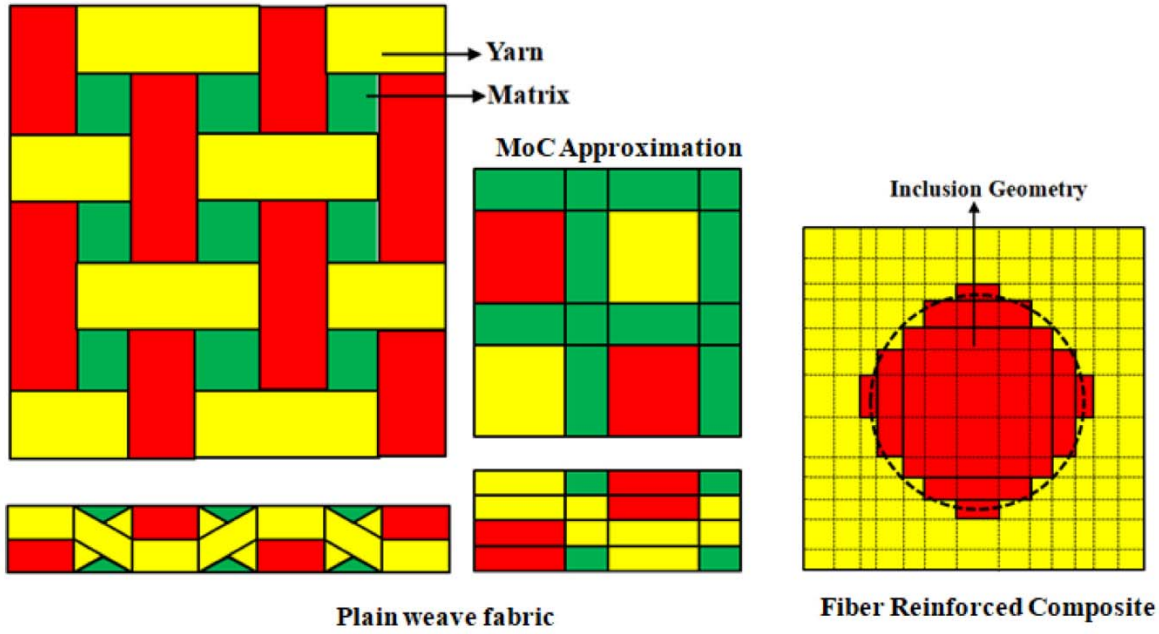

Fig. 1. A cell used in the MoCs approach to approximate plain weave and fiber-reinforced composite microstructures, and approximation of a circular fiber as a polygonal inclusion.

theory to predict elastic constants for fabrics. Barbero et al. [24], Blackketter et al. [25], Whitcomb [26] and Sun-Pui et al. [27] have used the FEM to construct unit cells to analyze fabrics. Wen and Aliabdi [28], and Li et al. [29] have used a meshless approach to study 3D fabrics. Tabiei and Jiang [30] and Tanov and Tabiei [31] have developed a micromechanics model for plain weave fabrics by dividing the unit cell into sub-cells and by enforcing continuity requirements at their interfaces. Though details of the microstructure can be accurately captured using the FEM and meshless approaches, they become difficult to use for large structures because of extensive computational resources needed.

Here we extend the capability of the FSA by employing wedge (penta-hedral) and cuboidal sub-volumes to analyze complex microstructures; this is similar to using penta- and hexa-hedral elements to discretize a structural geometry in 3-dimensional FEA. To facilitate analytical evaluation of quantities, we restrict sub-volumes to be right angled with orthogonal sides parallel to the global rectangular Cartesian coordinate axes. The formulation readily accommodates elastic–plastic behavior of its constituents and microstructure by using cuboidal and wedge sub-volumes, thereby making it suitable for a wide variety of applications.

The rest of the paper is organized as follows. The FSA formulation and derivation of expressions for strain concentration and transformation tensors are provided in Section 2 along with expressions for the stress and the stiffness matrix for the homogenized composite. In Section 3 we demonstrate the applicability and usefulness of the approach by analyzing inelastic deformations of unidirectional and woven fabric composites and comparing results to the corresponding ones in the literature. For unidirectional fiber reinforced composites, we study effects of the fiber geometry and the unit cell configuration (square edge, square diagonal and hexagonal close packing) on the predicted elastic constants and on its elastic–plastic deformations under transverse loading. The FSA is also used to predict elastic constants of plain and 2/2 twill weave composites. The strength predictions of weaves are made by using the Tsai–Wu failure criteria for the yarn and the von Mises criteria for the elastic–plastic resin pockets. Conclusions of the work are summarized in Section 4.

2. Micromechanics theory using the Fourier series analysis

2.1. Strain concentration and transformation matrices

Let the total infinitesimal strain (or strain increment) in a phase (fiber or matrix) be given by

$$\varepsilon_{ij}^{T} = \varepsilon_{ij}^{o} + \varepsilon_{ij} \tag{1}$$

where ε_{ij}^{o} and ε_{ij} are, respectively, the homogenized strain (or the average strain in an RVE) and the perturbation strain due to the presence of inclusions. Note that the volume averaged perturbed strain equals zero, i.e.,

$$\frac{1}{V}\int_{V} \varepsilon_{ij} dV = 0 \tag{2}$$

Following Walker et al. [12], we express constitutive equation for either the inclusion or the matrix as

$$\sigma_{ij} = \left\{ C_{ijkl}^{M} + \delta C_{ijkl} \right\} \left\{ \varepsilon_{kl}^{T} - \varepsilon_{kl}^{p} \right\} \tag{3}$$

where $\delta C_{ijkl} = \vartheta \left\{ C_{ijkl}^{F} - C_{ijkl}^{M} \right\}$, $\vartheta = 1(0)$ for the fiber (matrix), ε_{kl}^{p} is the plastic strain, and $C_{ijkl}^{F}, C_{ijkl}^{M}$ are 4^{th} order stiffness matrix for the fiber and the matrix, respectively. We rewrite Eq. (3) as

$$\sigma_{ij} = C_{ijkl}^{M} \left\{ \varepsilon_{kl}^{o} + \varepsilon_{kl} - \varepsilon_{kl}^{*} \right\} \tag{4a}$$

where the eigen-strain ε_{kl}^{*} is given by

$$C_{ijkl}^{M} \varepsilon_{kl}^{*} = C_{ijkl}^{M} \varepsilon_{kl}^{P} - \delta C_{ijkl} \left(\varepsilon_{kl}^{o} + \varepsilon_{kl} - \varepsilon_{kl}^{P} \right). \tag{4b}$$

Substituting for stresses in equilibrium equations, and noting that ε_{kl}^{o} is a constant, we get

$$C_{ijkl}^{M} \frac{\partial \varepsilon_{kl}}{\partial x_j} = C_{ijkl}^{M} \frac{\partial \varepsilon_{kl}^{*}}{\partial x_j} \tag{5}$$

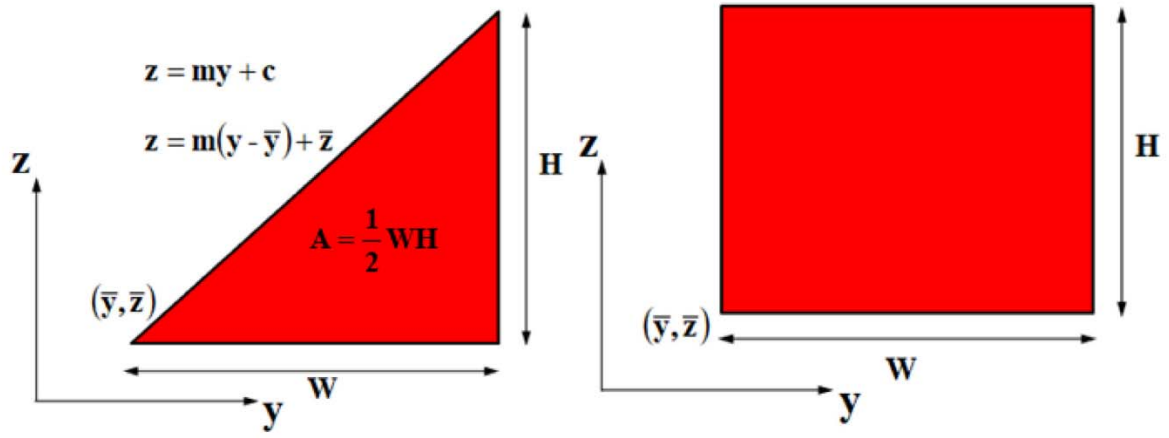

Fig. 2. Cross-section of a wedge and of a cuboidal sub-volume used in the FSA to capture inclusion's geometry.

Due to periodicity in the composite, we expand the displacement field $\mathbf{u}$ and the eigen-strain $\boldsymbol{\varepsilon}^*$ in Fourier series as

$$\begin{aligned} u_k &= \sum \sum_{0}^{\pm\infty'} \sum \hat{u}_k(\boldsymbol{\xi}) \exp(i\boldsymbol{\xi}\cdot\mathbf{r}), \\ &\text{where } \hat{u}_k(\boldsymbol{\xi}) = \frac{1}{V}\int_V u_k \exp(-i\boldsymbol{\xi}\cdot\mathbf{r})\,dV, \\ \varepsilon^*_{kl} &= \sum \sum_{0}^{\pm\infty'} \sum \hat{\varepsilon}^*_{kl}(\boldsymbol{\xi}) \exp(i\boldsymbol{\xi}\cdot\mathbf{r}), \\ &\text{where } \hat{\varepsilon}^*_{kl}(\boldsymbol{\xi}) = \frac{1}{V}\int_V \varepsilon^*_{kl} \exp(-i\boldsymbol{\xi}\cdot\mathbf{r})\,dV, \end{aligned} \tag{6}$$

$\pm\infty'$ indicates that $n = 0$ is excluded from the summation since $\hat{u}_k(\boldsymbol{\xi} = \mathbf{0})$ represents a rigid body displacement, and $\boldsymbol{\xi} = \{\xi_1, \xi_2, \xi_3\}$, $\xi_i = \frac{2\pi n_i}{L_i}$, $\mathbf{r} = \{x_1, x_2, x_3\}$ $V = L_1\ x\ L_2\ x\ L_3$, L_1, L_2 and L_3 equal sides of a cuboidal RVE.

Using Eqs. (5), (6) and the strain–displacement relations, we express $\hat{u}_k$ in terms of $\boldsymbol{\varepsilon}^*$in the Fourier space as

$$\hat{u}_k(\boldsymbol{\xi}) = \frac{-i}{|\boldsymbol{\xi}|^2} M^{-1}_{ik} C^M_{ijrs} \hat{\varepsilon}^*_{rs}(\boldsymbol{\xi}) \xi_j, \text{ where } |\boldsymbol{\xi}| = \sqrt{\xi_i \xi_i} \tag{7}$$

with $M_{ik} = C^M_{ijkl}\zeta_l\zeta_j$. Using Eqs. (4) and (7), we express strains in the physical space as

$$\begin{aligned} \varepsilon^T_{kl} &= \varepsilon^o_{kl} + \\ &\sum \sum_{0}^{\pm\infty'} \sum g_{klij} \left\{ \frac{1}{V}\int_V \left(C^M_{ijrs}\varepsilon^P_{rs}(\mathbf{r}') - \delta C_{ijrs}\left(\varepsilon^T_{rs}(\mathbf{r}') - \varepsilon^P_{rs}(\mathbf{r}')\right)\right) \right. \\ &\left. \times \exp\left(i\boldsymbol{\xi}\cdot\left[\mathbf{r}-\mathbf{r}'\right]\right) dV(\mathbf{r}') \right\} \end{aligned} \tag{8}$$

where $g_{klij} = \frac{1}{2}\left(M^{-1}_{ik}\zeta_j\zeta_l + M^{-1}_{il}\zeta_j\zeta_k\right)$ and $\boldsymbol{\zeta} = \frac{\boldsymbol{\xi}}{|\boldsymbol{\xi}|}$

The average strain $\boldsymbol{\varepsilon}^{T\beta}$ in the β^{th} sub-cell is given by

$$\varepsilon^{T\beta}_{rs} = \frac{1}{V^\beta}\int_{V^\beta} \varepsilon^T_{rs}(\mathbf{r}')\,dV(\mathbf{r}') \tag{9}$$

Using Eqs. (8) and (9), we get the following expression for the average strain in the αth sub-cell:

$$\begin{aligned} \varepsilon^{T\alpha}_{kl} = \varepsilon^o_{kl} &+ \sum_{\beta=1}^{N} f^\beta \left\{ \sum \sum_{0}^{\pm\infty'} \sum \left(g_{klij} C^M_{ijrs} Q^\alpha(\boldsymbol{\xi}) Q^\beta(-\boldsymbol{\xi}) \right) \right. \\ &\left. + \left(g_{klij}\delta C_{ijrs} Q^\alpha(\boldsymbol{\xi}) Q^\beta(-\boldsymbol{\xi}) \right) \right\} \varepsilon^P_{rs} \\ &- \sum_{\beta=1}^{N} f^\beta \left(\sum \sum_{0}^{\pm\infty'} \sum g_{klij}\delta C_{ijrs} Q^\alpha(\boldsymbol{\xi}) Q^\beta(-\boldsymbol{\xi}) \right) \varepsilon^T_{rs} \end{aligned} \tag{10}$$

where $Q^\alpha(\boldsymbol{\xi}) = \frac{1}{V^\alpha}\int_{V^\alpha} \exp(i\boldsymbol{\xi}\cdot\mathbf{r})\,dV(\mathbf{r})$, and $f^\beta = \frac{V^\beta}{V}$, the volume fraction of sub-cell β, which can either be the fiber or the matrix. We rewrite Eq. (10) as

$$\varepsilon^{T\alpha}_{kl} = \varepsilon^o_{kl} + \sum_{\beta=1}^{N} \left[f^\beta T^{\alpha\beta}_{klrs} \right] \varepsilon^P_{rs} - \sum_{\beta=1}^{N} \left[f^\beta S^{\alpha\beta}_{klrs} \right] \varepsilon^{T\beta}_{rs} \tag{11}$$

where $S^{\alpha\beta}_{klrs} = \sum \sum_0^{\pm\infty'} \sum g_{klij}\delta C_{ijrs} Q^\alpha(\boldsymbol{\xi}) Q^\beta(-\boldsymbol{\xi})$, and $T^{\alpha\beta}_{klrs} = \sum \sum_0^{\pm\infty'} \sum g_{klij} C^M_{ijrs} Q^\alpha(\boldsymbol{\xi}) Q^\beta(-\boldsymbol{\xi}) + S^{\alpha\beta}_{klrs}$.

Writing Eq. (11) for all N sub-cells of the RVE, we have

$$\begin{aligned} \begin{Bmatrix} \boldsymbol{\varepsilon}^{T1} \\ \boldsymbol{\varepsilon}^{T2} \\ \vdots \\ \boldsymbol{\varepsilon}^{TN} \end{Bmatrix} = \boldsymbol{\varepsilon}^T = &\begin{bmatrix} \mathbf{M^{11}} & \mathbf{M^{12}} & \cdots & \mathbf{M^{1N}} \\ \mathbf{M^{21}} & \mathbf{M^{22}} & \cdots & \mathbf{M^{2N}} \\ \vdots & \vdots & \vdots & \vdots \\ \mathbf{M^{N1}} & \mathbf{M^{N2}} & \cdots & \mathbf{M^{NN}} \end{bmatrix} \begin{Bmatrix} \boldsymbol{\varepsilon}^o \\ \boldsymbol{\varepsilon}^o \\ \vdots \\ \boldsymbol{\varepsilon}^o \end{Bmatrix} \\ &+ \begin{bmatrix} \mathbf{M^{11}} & \mathbf{M^{12}} & \cdots & \mathbf{M^{1N}} \\ \mathbf{M^{21}} & \mathbf{M^{22}} & \cdots & \mathbf{M^{2N}} \\ \vdots & \vdots & \vdots & \vdots \\ \mathbf{M^{N1}} & \mathbf{M^{N2}} & \cdots & \mathbf{M^{NN}} \end{bmatrix} \\ &\times \begin{bmatrix} \mathbf{f^1T^{11}} & \mathbf{f^2T^{12}} & \cdots & \mathbf{f^NT^{1N}} \\ \mathbf{f^1T^{21}} & \mathbf{f^2T^{22}} & \cdots & \mathbf{f^NT^{2N}} \\ \vdots & \vdots & \vdots & \vdots \\ \mathbf{f^1T^{N1}} & \mathbf{f^2T^{N2}} & \cdots & \mathbf{f^NT^{NN}} \end{bmatrix} \begin{Bmatrix} \boldsymbol{\varepsilon}^{p1} \\ \boldsymbol{\varepsilon}^{p2} \\ \vdots \\ \boldsymbol{\varepsilon}^{pN} \end{Bmatrix} \end{aligned} \tag{12}$$

where

$$\begin{bmatrix} \mathbf{M^{11}} & \mathbf{M^{12}} & \cdots & \mathbf{M^{1N}} \\ \mathbf{M^{21}} & \mathbf{M^{22}} & \cdots & \mathbf{M^{2N}} \\ \vdots & \vdots & \vdots & \vdots \\ \mathbf{M^{N1}} & \mathbf{M^{N2}} & \cdots & \mathbf{M^{NN}} \end{bmatrix} = \begin{bmatrix} \mathbf{I} + \mathbf{f^1S^{11}} & \mathbf{f^2S^{12}} & \cdots & \mathbf{f^NS^{1N}} \\ \mathbf{f^1S^{21}} & \mathbf{I} + \mathbf{f^2S^{22}} & \cdots & \mathbf{f^NS^{2N}} \\ \vdots & \vdots & \vdots & \vdots \\ \mathbf{f^1S^{N1}} & \mathbf{f^2S^{N2}} & \cdots & \mathbf{I} + \mathbf{f^NS^{NN}} \end{bmatrix}^{-1}$$

One can write Eq. (12) in the following alternative form:

$$\boldsymbol{\varepsilon}^T = [\mathbf{A}]\,\boldsymbol{\varepsilon}^o + [\mathbf{D}]\,\boldsymbol{\varepsilon}^p_S \tag{13a}$$

where the strain concentration and the transformation matrices, [**A**] and [**D**], given by Eq. (13b)

$$[\mathbf{A}] = \begin{bmatrix} \sum_{\alpha=1}^{N} \mathbf{M}^{1\alpha} \\ \sum_{\alpha=1}^{N} \mathbf{M}^{2\alpha} \\ \vdots \\ \sum_{\alpha=1}^{N} \mathbf{M}^{N\alpha} \end{bmatrix}, [\mathbf{D}] = \begin{bmatrix} \mathbf{M}^{11} & \mathbf{M}^{12} & \cdots & \mathbf{M}^{1N} \\ \mathbf{M}^{21} & \mathbf{M}^{22} & \cdots & \mathbf{M}^{2N} \\ \vdots & \vdots & \vdots & \vdots \\ \mathbf{M}^{N1} & \mathbf{M}^{N2} & \cdots & \mathbf{M}^{NN} \end{bmatrix} \times \begin{bmatrix} f^1\mathbf{T}^{11} & f^2\mathbf{T}^{12} & \cdots & f^N\mathbf{T}^{1N} \\ f^1\mathbf{T}^{21} & f^2\mathbf{T}^{22} & \cdots & f^N\mathbf{T}^{2N} \\ \vdots & \vdots & \vdots & \vdots \\ f^1\mathbf{T}^{N1} & f^2\mathbf{T}^{N2} & \cdots & f^N\mathbf{T}^{NN} \end{bmatrix} \tag{13b}$$

capture geometric effects of inclusions and their distributions through tensors $\mathbf{S}^{\alpha\beta}$ and $\mathbf{A}^{\alpha\beta}$. Eq. (13) is iteratively solved by initially assuming deformations to be elastic over the incremental load applied, finding plastic strain increments, and repeating the process within the same load step till strains have converged in all sub-cells. Subsequently, the macroscopic stresses in the RVE are calculated by volume averaging them over all sub-cells, i.e.,

$$\boldsymbol{\sigma}^{\mathrm{RVE}} = \sum_{\alpha=1}^{N} f^{\alpha}\boldsymbol{\sigma}^{\alpha} \tag{14}$$

2.2. Effective stiffness of the RVE

For elastic deformations, the stiffness matrix of the RVE derived by using Eq. (14) and constitutive equations is given by

$$\mathbf{C}^{\mathrm{RVE}} = \sum_{\alpha=1}^{N} f^{\alpha}\mathbf{C}^{\alpha} : \mathbf{A}^{\alpha} \tag{15}$$

For plastic deformations, we assume the additive decomposition of small strains into elastic and plastic parts, and follow Dvorak [32] to determine the instantaneous concentration tensors of the sub-cells. From the constitutive equation for the sub-cell $'\alpha'$, we get

$$\boldsymbol{\sigma}^{\alpha} = \mathbf{C}^{\alpha} : \boldsymbol{\varepsilon}^{\alpha} + \boldsymbol{\sigma}^{\mathrm{Re}\alpha}, \text{ and } \boldsymbol{\varepsilon}^{\alpha} = \mathbf{S}^{\alpha} : \boldsymbol{\sigma}^{\alpha} + \boldsymbol{\varepsilon}^{\mathrm{p}\alpha} \tag{16}$$

where the relaxation stress is given by

$$\boldsymbol{\sigma}^{\mathrm{Re}\alpha} = -\mathbf{C}^{\alpha} : \boldsymbol{\varepsilon}^{\mathrm{p}\alpha} \text{ or } \boldsymbol{\varepsilon}^{\mathrm{p}\alpha} = -\mathbf{S}^{\alpha} : \boldsymbol{\sigma}^{\mathrm{Re}\alpha} \tag{17}$$

From Eqs. (13) and (17) we get expression (18) for local strains in sub-cell $'\alpha'$.

$$\boldsymbol{\varepsilon}^{\alpha} = \left(\mathbf{I} + \sum_{\beta=1}^{N} \mathbf{D}^{\alpha\beta} : \mathbf{S}^{\alpha} : \mathbf{C}^{\mathrm{p}\alpha}\right)^{-1} : \mathbf{A}^{\alpha} : \boldsymbol{\varepsilon}^{\mathbf{RVE}} = \boldsymbol{A}^{\alpha} : \boldsymbol{\varepsilon}^{\mathbf{RVE}} \tag{18}$$

For inelastic deformations the concentration tensor $\boldsymbol{A}^{\alpha}$replaces $\mathbf{A}^{\alpha}$, and the elastic–plastic stiffness matrix replaces the elastic stiffness matrix in Eq. (15).

2.3. Determination of Q terms for wedge and cuboidal sub-volumes

The evaluation of the **S** and **T** tensors requires finding $\mathrm{Q}^{\alpha}(\xi)$ and $\mathrm{Q}^{\beta}(-\xi)$ terms for the sub-volume. In evaluating these, we consider seven different cases depending upon which components $[\xi_x, \xi_y, \xi_z]$ of the frequency vector ξ vanish, and exclude the null frequency vector since it corresponds to a rigid body displacement. Fig. 2 shows the cross-section and defines quantities $\overline{x}$, $\overline{y}$, $\overline{z}$, A, W, L, H and m that appear in the expression for Q for wedge and cuboidal sub-volumes, respectively, and Eq. (19) gives these expressions.

For wedge sub-volumes, upon integrating the expression for $\mathrm{Q}(\xi)$ given in Eq. (10), we get the following.

Case 1 $\xi_x \neq 0; \xi_y = 0; \xi_z = 0$

$$\mathrm{Q}(\xi)|_{\mathrm{WEDGE}} = \frac{1}{\mathrm{A}}\left\langle \mathrm{m}\frac{\mathrm{W}^2}{2}\right\rangle \cdot \frac{\sin\left(\xi_x\frac{\mathrm{L}}{2}\right)\exp\left(\mathrm{i}\xi_x\left[\overline{x}+\frac{\mathrm{L}}{2}\right]\right)}{\frac{\mathrm{L}}{2}\xi_x} \tag{19a}$$

Case 2: $\xi_x = 0; \xi_y \neq 0; \xi_z = 0$

$$\mathrm{Q}(\xi)|_{\mathrm{WEDGE}} = \frac{\mathrm{m}}{\mathrm{A}}\exp\left(\mathrm{i}\xi_y\overline{y}\right)\left\langle \exp\left(\mathrm{i}\xi_y\mathrm{W}\right)\left[\frac{1}{\xi_y^2} - \mathrm{i}\frac{\mathrm{W}}{\xi_y}\right] - \frac{1}{\xi_y^2}\right\rangle \tag{19b}$$

Case 3: $\xi_x = 0; \xi_y = 0; \xi_z \neq 0$

$$\mathrm{Q}(\xi)|_{\mathrm{WEDGE}} = \frac{\mathrm{i}}{\mathrm{A}}\frac{\exp\left(\mathrm{i}\xi_z\overline{z}\right)}{\xi_z}\left\langle \mathrm{W} + \mathrm{i}\frac{\exp\left(\mathrm{i}\xi_z\mathrm{mW}\right)-1}{\xi_z\mathrm{m}}\right\rangle \tag{19c}$$

Case 4: $\xi_x \neq 0; \xi_y \neq 0; \xi_z = 0$

$$\mathrm{Q}(\xi)|_{\mathrm{WEDGE}} = \frac{\mathrm{m}}{\mathrm{A}}\exp\left(\mathrm{i}\xi_y\overline{y}\right)\left\langle \exp\left(\mathrm{i}\xi_y\mathrm{W}\right)\left[\frac{1}{\xi_y^2} - \mathrm{i}\frac{\mathrm{W}}{\xi_y}\right] - \frac{1}{\xi_y^2}\right\rangle \times \frac{\sin\left(\xi_x\frac{\mathrm{L}}{2}\right)\exp\left(\mathrm{i}\xi_x\left[\overline{x}+\frac{\mathrm{L}}{2}\right]\right)}{\frac{\mathrm{L}}{2}\xi_x} \tag{19d}$$

Case 5: $\xi_x \neq 0; \xi_y = 0; \xi_z \neq 0$

$$\mathrm{Q}(\xi)|_{\mathrm{WEDGE}} = \frac{\mathrm{i}}{\mathrm{A}}\frac{\exp\left(\mathrm{i}\xi_z\overline{z}\right)}{\xi_z}\left\langle \mathrm{W} + \mathrm{i}\frac{\exp\left(\mathrm{i}\xi_z\mathrm{mW}\right)-1}{\xi_z\mathrm{m}}\right\rangle \times \frac{\sin\left(\xi_x\frac{\mathrm{L}}{2}\right)\exp\left(\mathrm{i}\xi_x\left[\overline{x}+\frac{\mathrm{L}}{2}\right]\right)}{\frac{\mathrm{L}}{2}\xi_x} \tag{19e}$$

Case 6: $\xi_x = 0; \xi_y \neq 0; \xi_z \neq 0$

$$\mathrm{Q}(\xi)|_{\mathrm{WEDGE}} = \frac{1}{\mathrm{A}}\frac{\exp\left(\mathrm{i}\xi_z\overline{z}\right)}{\xi_z}\exp\left(\mathrm{i}\xi_y\overline{y}\right) \times \left\{\left\langle \frac{\exp\left(\mathrm{i}\xi_y\mathrm{W}\right)-1}{\xi_y}\right\rangle - \left\langle \frac{\exp\left(\mathrm{i}\left[\xi_z\mathrm{m}+\xi_y\right]\mathrm{W}\right)-1}{\left[\xi_z\mathrm{m}+\xi_y\right]}\right\rangle\right\} \tag{19f}$$

Case 7: $\xi_x \neq 0; \xi_y \neq 0; \xi_z \neq 0$

$$\mathrm{Q}(\xi)|_{\mathrm{WEDGE}} = \frac{\sin\left(\xi_x\frac{\mathrm{L}}{2}\right)\exp\left(\mathrm{i}\xi_x\left[\overline{x}+\frac{\mathrm{L}}{2}\right]\right)}{\frac{\mathrm{L}}{2}\xi_x} \frac{1}{\mathrm{A}}\frac{\exp\left(\mathrm{i}\xi_z\overline{z}\right)}{\xi_z}\exp\left(\mathrm{i}\xi_y\overline{y}\right)\left\{\left\langle \frac{\exp\left(\mathrm{i}\xi_y\mathrm{W}\right)-1}{\xi_y}\right\rangle - \left\langle \frac{\exp\left(\mathrm{i}\left[\xi_z\mathrm{m}+\xi_y\right]\mathrm{W}\right)-1}{\left[\xi_z\mathrm{m}+\xi_y\right]}\right\rangle\right\} \tag{19g}$$

It is possible that when the slope m is an integer, then the term $\xi_z\mathrm{m}+\xi_y$ equals zero, and

$$\frac{\exp\left(\mathrm{i}\left[\xi_z\mathrm{m}+\xi_y\right]\mathrm{W}\right)-1}{\left[\xi_z\mathrm{m}+\xi_y\right]} = \mathrm{iW}.$$

Similarly, for cuboidal sub-volumes, we get the following for case 7.

$$\mathrm{Q}(\xi)|_{\mathrm{CUBOIDAL}} = \frac{\sin\left(\xi_x\frac{\mathrm{L}}{2}\right)}{\frac{\mathrm{L}}{2}\xi_x}\frac{\sin\left(\xi_y\frac{\mathrm{W}}{2}\right)}{\frac{\mathrm{W}}{2}\xi_y}\frac{\sin\left(\xi_z\frac{\mathrm{H}}{2}\right)}{\frac{\mathrm{H}}{2}\xi_z} \exp\left(\mathrm{i}\left[\xi_x\left(\overline{x}+\frac{\mathrm{L}}{2}\right)+\xi_y\left(\overline{y}+\frac{\mathrm{W}}{2}\right)+\xi_z\left(\overline{z}+\frac{\mathrm{H}}{2}\right)\right]\right) \tag{19h}$$

where $\left(\overline{x}+\frac{\mathrm{L}}{2}, \overline{y}+\frac{\mathrm{W}}{2}, \overline{z}+\frac{\mathrm{H}}{2}\right)$ is the location of the cuboidal element centroid. Here we have omitted expressions for $\mathrm{Q}(\xi)|_{\mathrm{CUBOIDAL}}$ for the remaining 6 cases. Recall that $\lim_{\xi_i\to 0}\frac{\sin\left(\xi_i\frac{\mathrm{L}}{2}\right)}{\frac{\mathrm{L}}{2}\xi_i} = 1$ where i is x, y or z.

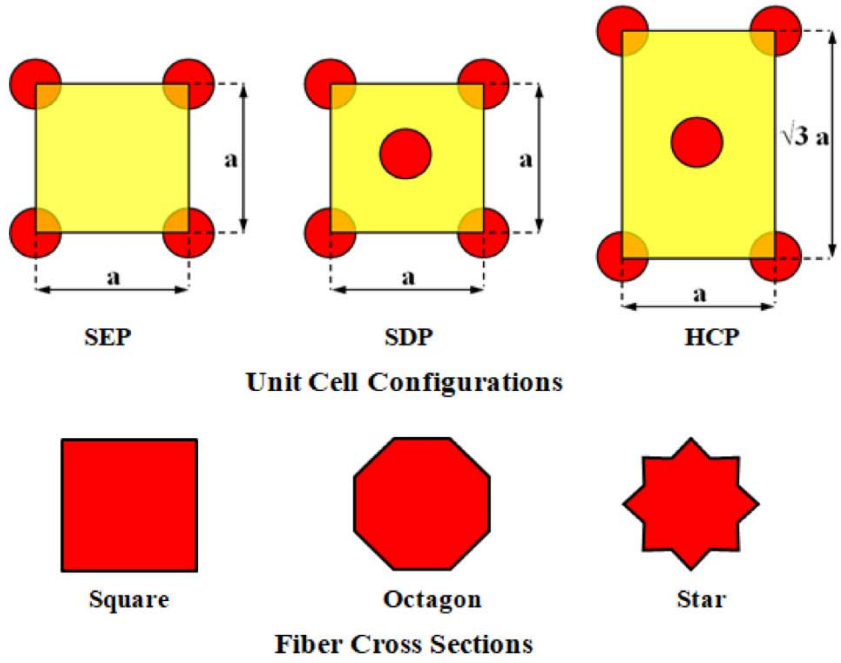

Fig. 3. Unit cell configurations and fiber cross-sections analyzed using the FSA.

Since tensors **S** and **T** are real, only real part of the product of $Q^{\alpha}(\xi)$ and $Q^{\beta}(-\xi)$ is considered and imaginary part is neglected.

2.4. Elasto-plastic analysis of uni-directional fiber-reinforced composite

Uni-directional fiber-reinforced composites are usually assumed to have two spatial length scales, one at the macro-level and the other at the micro-level consisting of fibers embedded in the surrounding matrix. Their elastic–plastic deformations are analyzed by assuming fibers to deform elastically and the matrix elasto-plastically obeying the von Mises yield criterion, the associated flow rule, and the Voce hardening law given by Eq. (20).

$$\mathrm{K}(\alpha) = \mathrm{k} + (\mathrm{Ro})\,\alpha + \mathrm{R}\left[1 - \exp(-\delta\alpha)\right] \tag{20}$$

Here α is the effective plastic strain. Definition of variables in Eq. (20) and its implementation is given in Gopinath and Batra [14].

Woven fabric composites have three spatial length scales, namely, a macro-scale, a sub-scale consisting of yarns embedded in the matrix, and a sub-sub-scale within the yarns. While analyzing fabrics using the FSA we consider only the first two length scales and disregard the third one by using homogenized yarns that are regarded as inclusions embedded in the matrix.

2.5. Progressive failure of woven fabric composite

The following two approaches are primarily employed to study progressive failure of composites; (1) continuum damage mechanics (CDM), and (2) equating damage variable equal to the inelastic (or the effective plastic) strain. In the CDM approach, the nonlinearity in the stress–strain response due to either individual or combined effects of matrix cracking, debonding, fiber breakage, etc. is captured by the accumulation and growth of damage, which is used to reduce elastic constants of the homogenized composite [33–35]. In the plasticity based approach, the nonlinearity in the stress–strain response is captured due to inelastic or plastic deformations. One way is to find a hardening law by curve fitting the effective stress-the effective plastic strain test data for a number of off-axis loading tests. This technique proposed by Sun and Chen [36] for unidirectional fiber reinforced composites was later employed for woven fabric composites, amongst others, by Ogihara and Reifsneider [37], Cho et al. [38] and Hufner [39]. We note that the hardening law incorporates nonlinearities associated with plastic deformations as well as failures that may occur in the composite during loading. As noted by Hufner [39], the nonlinearity in fabrics is primarily associated with matrix cracking. In a simpler plasticity-based approach, the material is assumed to be linearly elastic till failure. Once failure initiates the material undergoes inelastic deformations, usually softening. The problem is then formulated as elastic–plastic thereby tacitly taking the yield surface to represent the failure surface [34,40].

Implementing the CDM in conjunction with the FSA is difficult as there is no inelastic/eigen-strain defined in this approach. Furthermore, it requires generating concentration and transformation matrices at each load step when elastic constants of its constituents are degraded due to the accumulated damage. Hence, we use the plasticity based approach here.

Failure of the yarn (which essentially is a unidirectional fiber-reinforced composite) and of the pure resin pockets in the unit cell are modeled, respectively, by using the Tsai–Wu failure and the von Mises yield criteria. For both the resin and the yarn a linear softening law is used post-failure initiation and the closest point projection algorithm [41] is employed to integrate the elastic–plastic constitutive equations. Here, inelastic deformations are essentially used to capture softening response of the composite subsequent to failure initiation.

We describe modeling of inelastic deformations of a yarn in this subsection. Following van der Meer and Sluys [40], we write the failure surface for the composite yarn as

$$f(\boldsymbol{\sigma},\kappa)|_{\text{composite}} = \frac{1}{2}\boldsymbol{\sigma}\,\mathbf{P}(\kappa)|_{\text{composite}}\,\boldsymbol{\sigma} + \boldsymbol{\sigma}\,\mathbf{p}(\kappa)|_{\text{composite}} - 1 = 0 \tag{21}$$

Assuming '1' to be the fiber direction, we define

$$\mathbf{P}(\kappa)|_{\text{composite}} = \frac{\mathbf{P^o}}{h^2} \text{ and } \mathbf{p}(\kappa)|_{\text{composite}} = \frac{\mathbf{p^o}}{h}$$

$$\mathbf{P^o} = \begin{bmatrix} \frac{2}{F_{1t}F_{1c}} & -\frac{2}{\sqrt{F_{1t}F_{1c}F_{2t}F_{2c}}} & -\frac{2}{\sqrt{F_{1t}F_{1c}F_{2t}F_{2c}}} & 0 & 0 & 0 \\ & \frac{2}{F_{2t}F_{2c}} & -\frac{1}{F_{2t}F_{2c}} & 0 & 0 & 0 \\ & & \frac{2}{F_{2t}F_{2c}} & 0 & 0 & 0 \\ & & & \frac{1}{F_4^2} & 0 & 0 \\ & & & & \frac{1}{F_6^2} & 0 \\ & & & & & \frac{1}{F_6^2} \end{bmatrix},$$

$$\mathbf{p^o} = \begin{bmatrix} \frac{1}{F_{1t}} - \frac{1}{F_{1c}} \\ \frac{1}{F_{2t}} - \frac{1}{F_{2c}} \\ \frac{1}{F_{2t}} - \frac{1}{F_{2c}} \\ 0 \\ 0 \\ 0 \end{bmatrix} \tag{22}$$

Here, $\mathbf{p^o}$ and $\mathbf{P^o}$ are, respectively, the failure vector and the 6 x 6 matrix representing the Tsai–Wu failure criteria, and $h(\kappa) = 1 + \kappa H$ is the linear softening/hardening law for the composite with H being the softening/hardening modulus. (This H should not be confused with the H shown in Fig. 2.) In Eq. (22), F_{1t}/F_{1c} represents composite's fiber strength in tension/compression, F_{2t}/F_{2c} represents composite's matrix strength in tension/compression and F_4, F_6 represents composite's matrix shear strengths. The evolution of the internal variable κ is given by, $\Delta\kappa = \sqrt{\Delta\boldsymbol{\varepsilon}^{\mathbf{p}}\,[\mathbf{Q}]\,\Delta\boldsymbol{\varepsilon}^{\mathbf{p}}}$ where the right-hand-side represents the equivalent plastic strain as $[\mathbf{Q}]$ is the diagonal matrix $[1, 1, 1, 0.5, 0.5, 0.5]$.

The constitutive relation for the composite and the flow rule is given by

$$\boldsymbol{\sigma} = \mathbf{C} : \left(\boldsymbol{\varepsilon} - \boldsymbol{\varepsilon}^{\mathbf{p}}\right) \tag{23a}$$

$$\dot{\boldsymbol{\varepsilon}}^{\mathbf{p}} = \gamma \frac{\partial f(\boldsymbol{\sigma}, \kappa)}{\partial \boldsymbol{\sigma}} = \gamma \mathbf{m} \tag{23b}$$

The evolution of the plastic strain follows the Kuhn–Tucker relation

$$f \le 0,\ \dot{\gamma} \ge 0,\ f\dot{\gamma} = 0 \tag{24}$$

The integration of the elastic–plastic constitutive equations is performed by using the Newton–Raphson technique following the closest point projection algorithm [41].

The unknown plastic strain in Eq. (23b) in the $(n+1)^{th}$ time step is written as

$$\boldsymbol{\varepsilon}^{\mathbf{p}}_{\mathbf{n+1}} = \boldsymbol{\varepsilon}^{\mathbf{p}}_{\mathbf{n}} + \Delta\gamma \mathbf{m}_{\mathbf{n+1}} \tag{25}$$

We write the residue, $\mathbf{R}_{\mathbf{n+1}}$, for Eq. (25) as

$$\mathbf{R}_{\mathbf{n+1}} = -\boldsymbol{\varepsilon}^{\mathbf{p}}_{\mathbf{n+1}} + \boldsymbol{\varepsilon}^{\mathbf{p}}_{\mathbf{n}} + \Delta\gamma \mathbf{m}_{\mathbf{n+1}} \tag{26}$$

Linearizing $\mathbf{R}_{\mathbf{n+1}}$ for small increments in the variables gives

$$\mathbf{R}_{\mathbf{n+1}} + \frac{d\mathbf{R}_{\mathbf{n+1}}}{d\boldsymbol{\sigma}_{\mathbf{n+1}}} d\boldsymbol{\sigma}_{\mathbf{n+1}} + \frac{d\mathbf{R}_{\mathbf{n+1}}}{d\Delta\gamma} d\Delta\gamma = 0 \tag{27}$$

The yield surface for the $(n+1)^{th}$ load step is also linearized as

$$f(\boldsymbol{\sigma}, \kappa) + \frac{\partial f}{\partial \boldsymbol{\sigma}_{\mathbf{n+1}}} d\boldsymbol{\sigma}_{\mathbf{n+1}} + \frac{\partial f}{\partial \Delta\gamma} d\Delta\gamma = 0 \tag{28}$$

Pre-multiplying Eq. (27) with $\left[\frac{\partial f}{\partial \boldsymbol{\sigma}_{\mathbf{n+1}}}\right]\left[\frac{d\mathbf{R}_{\mathbf{n+1}}}{d\boldsymbol{\sigma}_{\mathbf{n+1}}}\right]^{-1}$ and substituting for $\left[\frac{\partial f}{\partial \boldsymbol{\sigma}_{\mathbf{n+1}}}\right] d\boldsymbol{\sigma}_{\mathbf{n+1}}$ we get

$$d\Delta\gamma = \frac{f(\boldsymbol{\sigma}, \kappa) - \left[\frac{\partial f}{\partial \boldsymbol{\sigma}_{\mathbf{n+1}}}\right]\left[\frac{d\mathbf{R}_{\mathbf{n+1}}}{d\boldsymbol{\sigma}_{\mathbf{n+1}}}\right]^{-1}\{\mathbf{R}_{\mathbf{n+1}}\}}{\left[\frac{\partial f}{\partial \boldsymbol{\sigma}_{\mathbf{n+1}}}\right]\left[\frac{d\mathbf{R}_{\mathbf{n+1}}}{d\boldsymbol{\sigma}_{\mathbf{n+1}}}\right]^{-1}\left\{\frac{d\mathbf{R}_{\mathbf{n+1}}}{d\Delta\gamma}\right\} - \frac{\partial f}{\partial \Delta\gamma}} \tag{29}$$

Stresses, strains, and the hardening parameter are then updated as

$$\begin{aligned} \{d\boldsymbol{\sigma}_{\mathbf{n+1}}\} &= -\left[\frac{d\mathbf{R}_{\mathbf{n+1}}}{d\boldsymbol{\sigma}_{\mathbf{n+1}}}\right]^{-1}\left\langle\left\{\frac{d\mathbf{R}_{\mathbf{n+1}}}{d\Delta\gamma}\right\} d\Delta\gamma + \{\mathbf{R}_{\mathbf{n+1}}\}\right\rangle \\ d\boldsymbol{\varepsilon}^{\mathbf{p}}_{\mathbf{n+1}} &= -\mathbf{C}^{-1} : d\boldsymbol{\sigma}_{\mathbf{n+1}} \\ \left\{\boldsymbol{\varepsilon}^{\mathbf{p}}_{\mathbf{n+1}}\right\} &= \left\{\boldsymbol{\varepsilon}^{\mathbf{p}}_{\mathbf{n+1}}\right\} + \left\{d\boldsymbol{\varepsilon}^{\mathbf{p}}_{\mathbf{n+1}}\right\} \\ \Delta\gamma &= \Delta\gamma + d\Delta\gamma \\ \kappa_{n+1} &= \kappa_n + \Delta\gamma\sqrt{\mathbf{m}\,[\mathbf{Q}]\,\mathbf{m}} \end{aligned} \tag{30}$$

For elastic–plastic deformations, we take Eq. (21) to represent the yield surface, and follow the preceding analysis. When the solution has converged, we deduce the following from Eqs. (23) and (26)

$$d\boldsymbol{\sigma}_{\mathbf{n+1}} = \Xi\left\{d\boldsymbol{\varepsilon}_{\mathbf{n+1}} - d\Delta\gamma\left\langle\mathbf{m}_{\mathbf{n+1}} + \Delta\gamma\frac{\partial \mathbf{m}_{\mathbf{n+1}}}{\partial\Delta\gamma}\right\rangle\right\} \tag{31}$$

where $\Xi = \left\langle\mathbf{C}^{-1} + \Delta\gamma\frac{\partial \mathbf{m}_{\mathbf{n+1}}}{\partial \boldsymbol{\sigma}_{\mathbf{n+1}}}\right\rangle^{-1}$.

Substituting for $d\sigma_{n+1}$ from Eq. (31) into Eq. (28) we get

$$d\Delta\gamma = \frac{\mathbf{m}_{\mathbf{n+1}} : \Xi d\boldsymbol{\varepsilon}_{\mathbf{n+1}}}{\mathbf{m}_{\mathbf{n+1}} : \Xi\left\langle\mathbf{m}_{\mathbf{n+1}} + \Delta\gamma\frac{\partial \mathbf{m}_{\mathbf{n+1}}}{\partial\Delta\gamma}\right\rangle - \frac{\partial f}{\partial\Delta\gamma}} \tag{32}$$

Substituting from Eq. (32) in Eq. (31) we get

$$d\boldsymbol{\sigma}_{\mathbf{n+1}} = \left\{\Xi - \frac{\Xi\left\langle\mathbf{m}_{\mathbf{n+1}} + \Delta\gamma\frac{\partial \mathbf{m}_{\mathbf{n+1}}}{\partial\Delta\gamma}\right\rangle \otimes \left\langle\Xi\mathbf{m}_{\mathbf{n+1}}\right\rangle^{t}}{\mathbf{m}_{\mathbf{n+1}} : \Xi\left\langle\mathbf{m}_{\mathbf{n+1}} + \Delta\gamma\frac{\partial \mathbf{m}_{\mathbf{n+1}}}{\partial\Delta\gamma}\right\rangle - \frac{\partial f}{\partial\Delta\gamma}}\right\} d\boldsymbol{\varepsilon}_{\mathbf{n+1}} \tag{33}$$

We note the asymmetry in the stiffness matrix due to the presence of the term $\frac{\partial \mathbf{m}_{\mathbf{n+1}}}{\partial\Delta\gamma}$, which was also mentioned in [40].

We follow the same approach as above for failure of resin pockets in which the yarn is embedded by taking the following failure surface

$$f(\boldsymbol{\sigma}, \kappa)|_{\text{matrix}} = \sqrt{\frac{3}{2}\mathbf{s} : \mathbf{s}} - Y_{\text{matrix}} - H\kappa = 0 \tag{34}$$

where s is the deviatoric stress tensor, and Y_{matrix} and H are the failure strength and the softening/hardening modulus, respectively.

3. Prediction of elastic moduli

3.1. Effect of fiber shape and unit cell configuration on elastic–plastic analysis of fiber-reinforced composite

Though modern manufacturing methods have allowed production of noncircular fibers, there have been very limited studies on characterizing effects of fiber shape on the response of composites [43]. Both experiments and numerical studies have shown that fiber shape significantly influences composite's response. Pathan et al. [43] studied damping characteristics of circular, elliptical, triangular and star shaped fibers. Agnese and Scarpa [44] experimentally showed a significant increase in damping properties of star shaped fibers compared to that of circular fibers. Paknia et al. [45] studied the effect of size and shape of Silica-Carbide particles in aluminum matrix. Out of square, circular and triangular shaped reinforcements considered, they found that circular cross section provided the softest elastic–plastic response in comparison to square and triangular cross section reinforcements. Brockenbrough et al. [42,46] studied the effect of fiber shape and unit cell configuration on the inelastic response of metal matrix composites. Herraez et al. [47] found that composites with lobular fibers exhibited superior strength than those with circular fibers under transverse

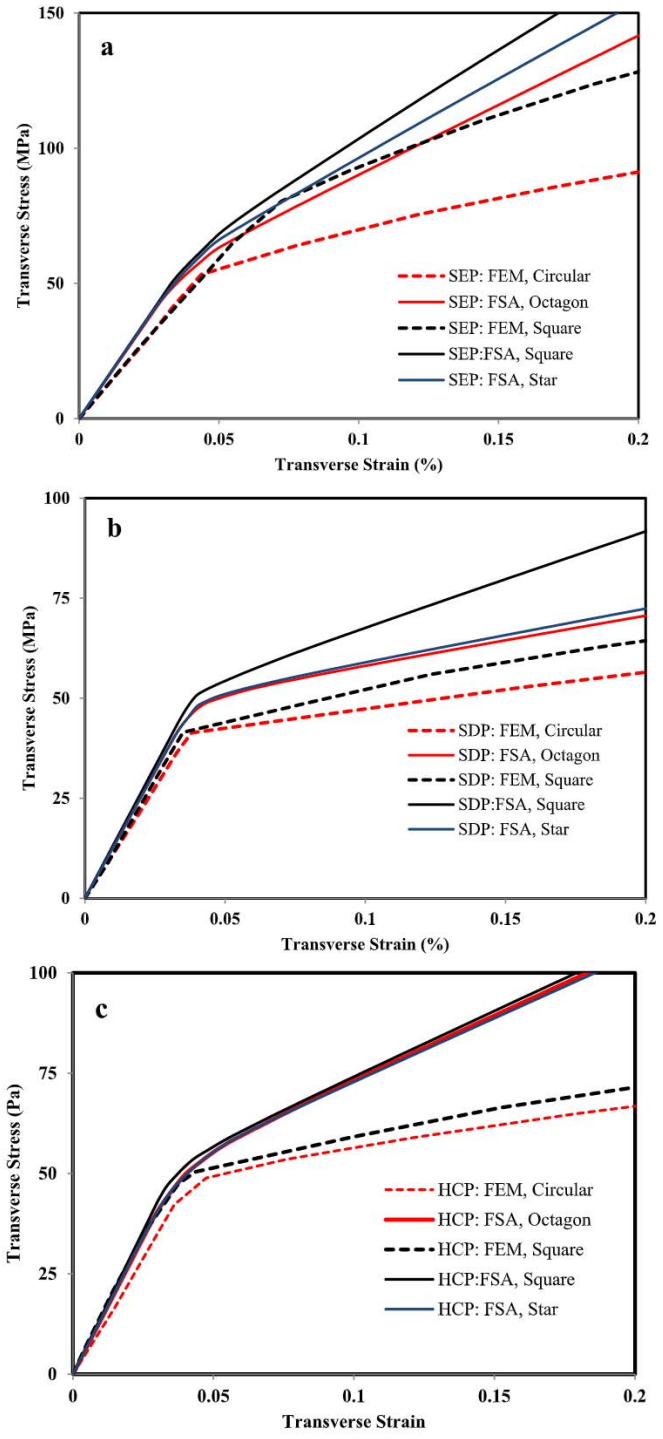

Fig. 4. a–c: Sensitivity of the elastic–plastic response to SEP, SDP and HCP configurations having square, octagonal and star-shaped fibers. The FEM results are from Brockenbrough et al. [42].

compression, while Yang et al. [48] showed that triangular fibers had higher elastic modulus and strength than their circular counterparts. Yang et al. [49] showed that gear shaped fibers had significantly higher strength than circular fibers.

Here we use the FSA to study the effect of fiber shape and unit cell configuration on the elastic–plastic response of a fiber-reinforced composite. Square edge packing (SEP), hexagonal close-packing (HCP) and square-diagonal packing (SDP) unit cell configurations having square, circular and star shaped fibers (as shown in Fig. 3) are employed

Table 1
Values of elastic constants for Aluminum matrix and Boron fibers.

Aluminum-6061 O		Boron	
E	ν	E	ν
69 GPa	0.33	410 GPa	0.2

Table 2
Voce hardening parameters for Aluminum-6061.

k (yield stress)	Ro	R	δ
43 MPa	30 MPa	72 MPa	35

to study Boron-Aluminum fiber-reinforced composite under transverse loading. This composite system with 46% fiber volume fraction was previously analyzed by Brockenbrough et al. [42,46] using the FEM, and by Gopinath and Batra [14] with three micro-mechanics techniques, including the FSA but with only square fibers and cuboidal sub-cells. In [14] we used the transformation field analysis to study the effect of fiber cross-section on composite's elastic–plastic response. Here we employ the FSA and consider circular (approximated by octagonal) and star shaped fibers.

Elastic constants of the constituents given in Brockenbrough et al. [42] are listed in Table 1. We assume Aluminum and Boron fibers to, respectively, deform elasto-plastically and elastically. The von Mises yield criteria with the associated flow rule and the Voce hardening law (given by Eq. (20)) govern plastic deformations of the Aluminum. Values of hardening parameters are listed in Table 2 [14]. All analyses are carried out using approximately 150 to 160 sub-cells. In Table 3 we have compared elastic constants predicted from the FSA using Eq. (15) for the three fiber shapes and the 3 unit cell configurations with those reported by Brockenbrough et al. It is clear that the transverse elastic modulus and the shear moduli are sensitive to changes in the unit cell configuration and the fiber shape. The SEP arrangement with square fibers gives the highest values while the SDP arrangement with octagonal fibers the least. The elastic constants for star shaped fibers fall in between those for the square and the octagonal fibers. Values of G_L are unaffected by both the packing arrangement and the fiber cross-section, but those of ν_L, E_L and G_T strongly depend upon them.

In Fig. 4 we compare the elastic–plastic response for the three fiber cross-sections for each of the three unit-cell configurations under transverse loading. The SEP (SDP) fiber arrangement gives the stiffest (softest) response and the HCP arrangement falls in-between that for the SEP and the SDP fiber arrangements. Looking at the response for the three fiber shapes, we see that square fibers have a stiffer response than the octagonal fibers for all packing arrangements and the response of star shaped fibers falls in between that of the square and the circular fibers for all three unit-cell arrangements. As seen from the figure the trends mimic those from the FEA but the FSA predicts more hardening than that given by the FEM.

The sensitivity of the elastic–plastic response to the fiber geometry and packing arrangements can be explained by examining the local plastic strains and the hydrostatic stress within the unit cell due to transverse loading [14]. Figs. 5 and 6 depict, respectively, for a macro-strain of 0.25%, fringe plots of the effective plastic strain and of the hydrostatic stress in the square edge and diagonal arrangements. These plots were generated using MATLAB's grid-data interpolation function using field variables at centroids of the sub-cell locations. White border lines indicate the fiber location within the unit cell. The imposed periodic boundary conditions and the symmetric arrangement of fibers within the unit cell about the XY- and the XZ-planes (the X-axis is along the fibers) result in symmetric contour plots of the field variables about these planes. From the contour plots we see that for the SEP arrangement magnitudes of the effective plastic strain increase as we go from the square ⇒ star ⇒ octagonal fibers. This is attributed to the buildup of the hydrostatic stress along surfaces of the fibers which

Table 3
Effect of fiber geometry and unit cell configuration on predicted values of elastic constants.

		E_L(GPa)	ν_L	E_T(GPa)	G_T(GPa)	G_L(GPa)
Packing arrangement	Experiment	228	0.24	138	57	
Square edge packing (SEP)	FEM-Square	228	0.266	153	60	
	FEM-Circular	228	0.263	152	57	
	FSA-Square	226	0.263	152	44	53
	FSA-Octagon	226	0.263	149	45	53
	FSA-Star	226	0.262	151	45	55
Hexagonal close packing (HCP)	FEM-Square	228	0.263	138	50	
	FEM-Circular	227	0.262	137	50	
	FSA-Square	226	0.262	140	51	56
	FSA-Octagon	226	0.263	136	50	53
	FSA-Star	226	0.262	138	51	54
Square diagonal packing (SDP)	FEM-Square	227	0.262	134	48	
	FEM-Circular	227	0.24	138	45	
	FSA-Square	226	0.26	132	58	53
	FSA-Octagon	226	0.263	126	57	53
	FSA-Star	226	0.262	127	57	54

Table 4a
Elastic constants for plain weave fabric predicted using FSA.

Plain weave

E-Glass/epoxy [9,24]

Elastic constants						Geometric parameters		
	E_{11} (GPa)	E_{22} (GPa)	G_{12} (GPa)	ν_{12}	ν_{23}	V_f/V_c	V_f/V_y	θ
Yarn	47.77	18.02	3.88	0.314	0.249	0.35	0.65	9.5
	E (GPa)	ν						
Matrix	3.5	0.35						

Method	E_{xx}/E_{yy} (GPa)	E_{zz} (GPa)	G_{xz}/G_{yz} (GPa)	G_{xy} (GPa)	ν_{xz}/ν_{yz}	ν_{xy}
MoCs 1-step [9]	13.1	9.42	2.53	2.46	0.307	0.246
MoCs 2-step [9]	18.1	9.85	2.54	2.76	0.318	0.177
Tanov & Tabiei [24]	17.85	9.79	2.5	3.53	0.332	0.172
FSA	**17.3**	**9.76**	**2.46**	**2.31**	**0.332**	**0.179**
% diff FSA vs [24]	3%	0.3%	1.5%	34%	0%	4%

Graphite/epoxy [9,24]

Elastic constants						Geometric parameters		
	E_{11} (GPa)	E_{22} (GPa)	G_{12} (GPa)	ν_{12}	ν_{23}	V_f/V_c	V_f/V_y	θ
Yarn	137.3	10.79	5.394	0.26	0.46	0.38	0.65	1.4
	E (GPa)	ν						
Matrix	4.511	0.38						

Method	E_{xx}/E_{yy} (GPa)	E_{zz} (GPa)	G_{xz}/G_{yz} (GPa)	G_{xy} (GPa)	ν_{xz}/ν_{yz}	ν_{xy}
MoCs 1-step [9]	14.2	8.11	2.75	2.99	0.46	0.131
MoCs 2-step [9]	45.08	10.12	2.76	3.24	0.464	0.056
Tanov & Tabiei [24]	45.08	10.12	2.76	3.82	0.464	0.056
FSA	**45.0**	**10.1**	**2.83**	**3.47**	**0.464**	**0.058**
% diff FSA vs [24]	0.2%	0.1%	2.5%	9.2%	0%	3.5%

E-Glass/Vinylester [23]

Elastic constants						Geometric parameters		
	E_{11} (GPa)	E_{22} (GPa)	$G_{12}\backslash G_{23}$ (GPa)	ν_{12}	ν_{23}	V_f/V_c	V_f/V_y	θ *
Yarn	57.5	18.8	7.44/7.26	0.25	0.29	0.8	0.55	10.5
	E (GPa)	ν						
Matrix	3.4	0.35						

Method	E_{xx}/E_{yy} (GPa)	E_{zz} (GPa)	G_{xz}/G_{yz} (GPa)	G_{xy} (GPa)	ν_{xz}/ν_{yz}	ν_{xy}
Expt. [23]	24.8	8.5	4.2	6.5	0.28	0.1
Analytical [23]	25.33	13.46	5.24	5.19	0.29	0.12
FSA	**24.4**	**12.7**	**3.7**	**4.12**	**0.306**	**0.137**
% diff FSA vs Expt.	1.6%	33%	12%	37%	7%	37%

Table 4b
Elastic constants for 2/2 twill weave fabric predicted using FSA.

2/2 Twill weave									
S2-Glass/C50 [50]									
	Elastic constants						Geometric parameters		
	E_{11} (GPa)	E_{22} (GPa)	G_{12} (GPa)	G_{23} (GPa)	ν_{12}		ν_{23}	V_y/V_c	$\theta*$
Yarn	71.6	23.7	10.2	8.4	0.22		0.27	0.64	7
	E (GPa)	ν							
Matrix	3.45	0.35							
Method		E_{xx}/E_{yy} (GPa)	E_{zz} (GPa)	G_{xz}/G_{yz} (GPa)		G_{xy} (GPa)	ν_{xz}/ν_{yz}		ν_{xy}
Expt. [50]		28.7				–	0.1366		
Analytical [50]		30.6				6.83	0.1327		
FSA		**29.7**	**14.3**	**3.62**		**4.71**	**0.283**		**0.118**
% diff FSA vs Expt.		3.5%					70%		4%
E-Glass/Epoxy [23]									
	Elastic constants						Geometric parameters		
	E_{11} (GPa)	E_{22} (GPa)	G_{12} (GPa)	G_{23} (GPa)	ν_{12}	ν_{23}	V_f/V_y	V_f/V_y	$\theta*$
Yarn	55.7	18.5	6.89	6.04	0.22	0.34	0.75	0.38	6.5
	E (GPa)	ν							
Matrix	3.2	0.38							
Method		E_{xx}/E_{yy} (GPa)	E_{zz} (GPa)	G_{xz}/G_{yz} (GPa)		G_{xy} (GPa)	ν_{xz}/ν_{yz}		ν_{xy}
Expt. [33]		19.2		–		3.6			0.13
Analytical [33]		19.54	10.92	3.78		3.92	0.305		0.122
FSA		**19.2**	**9.91**	**2.37**		**2.78**	**0.355**		**0.14**
% diff FSA vs Expt.		0%				29.5%			7.8%
E-Glass/Polyethylene/Epoxy hybrid [23]									
	Elastic constants						Geometric parameters		
E-glass	E_{11} (GPa)	E_{22} (GPa)	G_{12} (GPa)	G_{23} (GPa)	ν_{12}	ν_{23}	V_f/V_y	V_f/V_y	$\theta*$
Yarn	55.7	18.5	6.89	6.04	0.22	0.34	0.75	0.32	17
	E (GPa)	ν							
Matrix	3.2	0.38							
PE	E_{11} (GPa)	E_{22} (GPa)	G_{12} (GPa)	G_{23} (GPa)	ν_{12}	ν_{23}	V_f/V_y	V_f/V_y	$\theta*$
Yarn	11.1	9.22	3.26	3.25	0.39	0.39	0.75	0.2	17
Method		E_{xx}/E_{yy} (GPa)	E_{zz} (GPa)	G_{xz}/G_{yz} (GPa)		G_{xy} (GPa)	ν_{xz}/ν_{yz}		ν_{xy}
Expt. [23]		18		3.5					0.13
Analytical [23]		19.95	12.84	4.51		4.36	0.33		0.165
FSA		**17.9**	**10.9**	**3.0**		**3.2**	**0.374**		**0.171**
% diff FSA vs Expt.		0.6%		1.7%					31%

limits plastic flow of the material. For the SDP arrangement, the plastic strains are comparable but the hydrostatic stress for square fiber is almost twice of that for the star and the octagonal fibers.

Regarding differences in the fiber arrangement on the elastic–plastic response, we see that though the magnitude of the maximum plastic strain observed in the SEP is either higher or comparable to that for the SDP, the hydrostatic stresses are an order of magnitude higher. Thus, regions of high magnitudes of plastic strains in the SEP are more localized. The geometric constraints imposed by the relatively stiff fibers in terms of the buildup of the hydrostatic stress and the plastic flow of the matrix help explain why the SDP arrangement with octagonal fibers shows much softer response than that exhibited by the SEP arrangement with square fibers. Further details on the effect of the shape and the packing arrangement are provided in [14].

3.2. Prediction of elastic constants of woven fabric composite

Woven fabric composites offer a number of advantages over non-woven/non-crimp laminates. The interlocking of yarns provides better reinforcement in the out of plane direction giving it higher delamination and impact resistance. Woven fabrics can also be easily molded and draped into complex shapes reducing manufacturing cost. The disadvantage, however, is reduction in stiffness and strength in the plane of the laminate due to crimping of fibers in the yarn. Since they form an important class of composites we explore using the FSA in predicting their stiffness and strength by neglecting their crimping.

We consider here plain and 2/2 twill weave composites shown in Fig. 7; other weaves like the 5H and 8H satin can be constructed in a similar manner with the unit cell sub-divided into many more sub-cells to accommodate the pattern. We assume the yarn cross-section to be rectangular with the geometric and material constants of yarns in the warp and the weft directions to be the same. We simplify the problem by assuming that there is no interstitial matrix present at cross-over points between the warp and the weft yarns. The unit cell dimensions for the FSA approach are taken to be $1 \times 1 \times 2t$ with t being the yarn thickness. Sub-cell dimensions, determined from the volume fraction, V_f, of the fiber in the yarn and the composite, and the yarn crimp

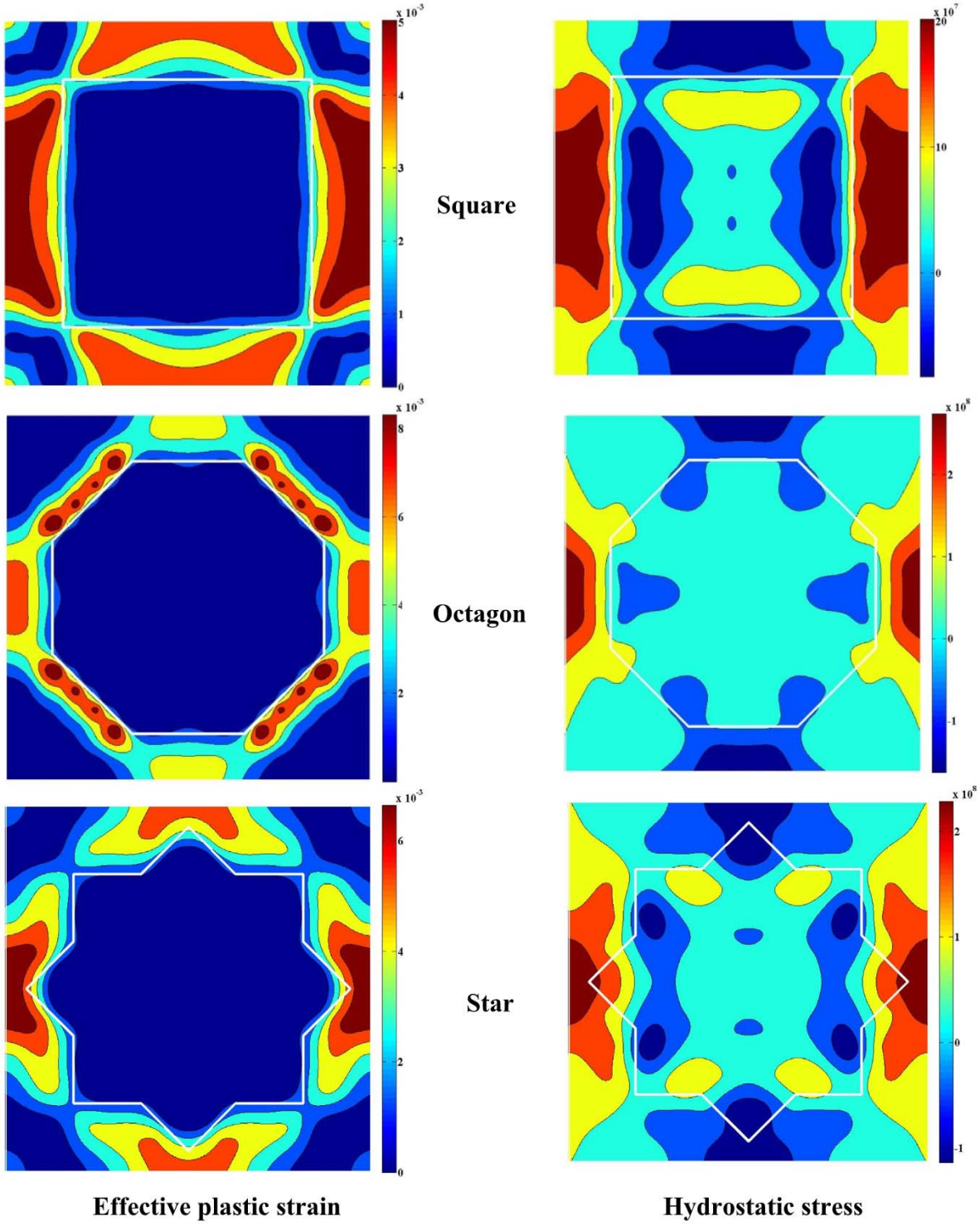

Fig. 5. Fringe plots of the effective plastic strain and the hydrostatic stress for square, octagonal and star cross-section fibers in the SEP arrangement.

(inclination angle), are given in Eq. (35) and are depicted in Fig. 7. The plain and the 2/2 twill weaves are constructed with approximately 50 and 150 sub-cells, respectively, making use of wedges and cuboids (see Fig. 7).

$$W_{\text{plain weave}} = \frac{1}{2}\frac{V_f \text{ in Composite}}{V_f \text{ in Yarn}} d_{\text{plain weave}} = \frac{(1-2W)}{2} t_{\text{plain weave}} = d\tan(\theta) \tag{35a}$$

$$W_{\text{twill weave}} = \frac{1}{4}\frac{V_f \text{ in Composite}}{V_f \text{ in Yarn}} d_{\text{twill weave}} = \frac{(1-4W)}{4} t_{\text{twill weave}} = d\tan(\theta) \tag{35b}$$

While analyzing fabrics using the FSA, the yarn is taken as inclusions in the matrix. Elastic constants from the FSA are predicted using Eq. (15). All relevant material constants and geometric parameters are listed in Table 4 along with elastic constants predicted from

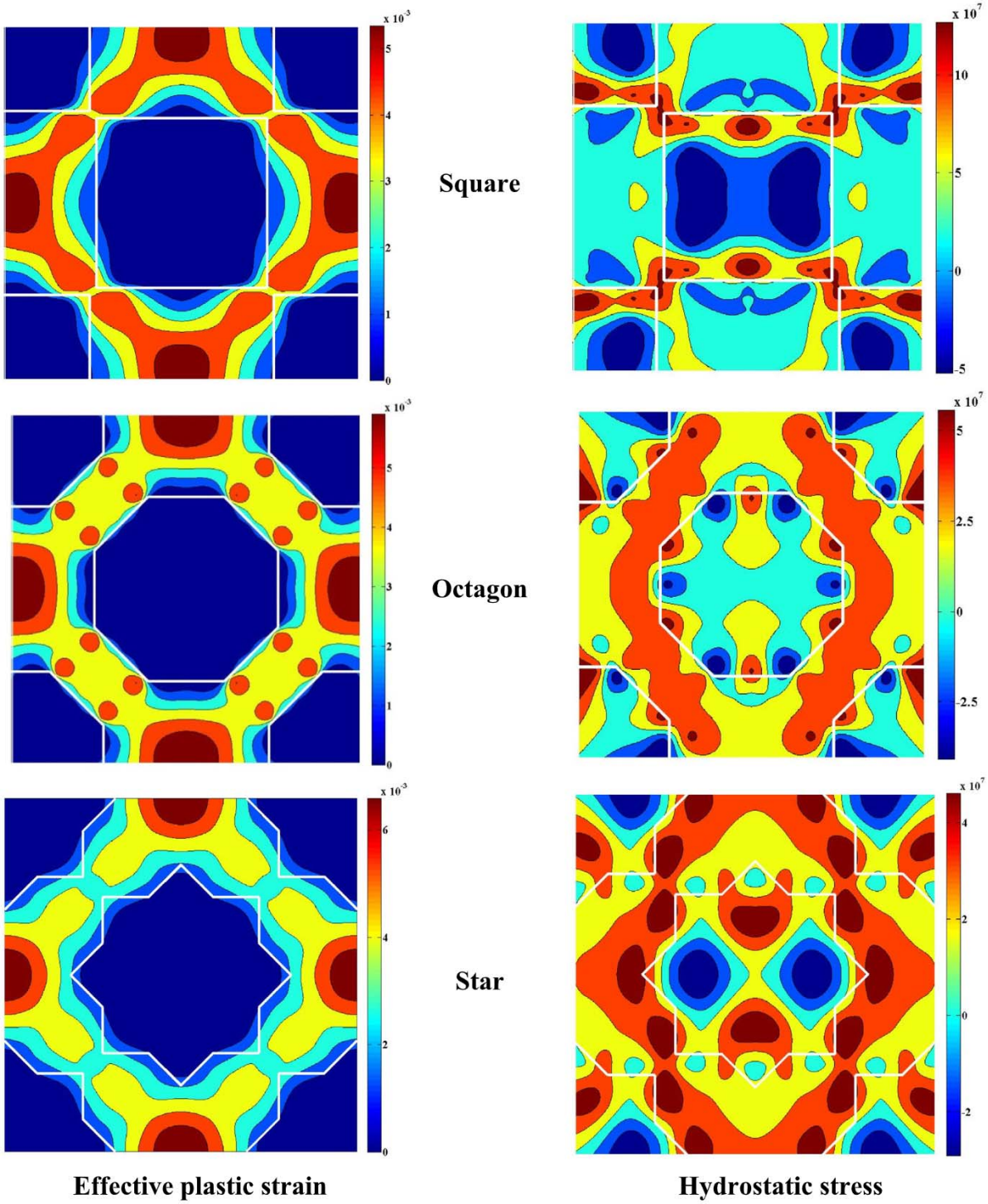

Fig. 6. Fringe plots of the effective plastic strain and the hydrostatic pressure for square, octagonal and star cross-section fibers in the SDP arrangement.

the FSA and those from other techniques. In Table 4, θ^* for the E-glass/vinylester plain weave and twill weaves indicates the crimp angle estimated from the unit cell dimensions provided in the references.

3.3. Prediction of elastic constants of fiber-reinforced composite

For square edge packing (SEP) and square diagonal packing (SDP) arrangements with square and octagonal fibers, the predicted elastic constants (except for the longitudinal modulus that is accurately predicted by all methods) for fiber-reinforced composites for $V_f = 0.15$, 0.3, 0.46 and 0.6 for Aluminum matrix and Boron fibers [37] are compared in Fig. 8 with those from the concentric cylinder model and the test data [51]. For small volume fractions the predicted transverse elastic modulus and the shear moduli are close to each other and to their experimental values indicating that they become independent of the fiber cross-section and packing arrangement.

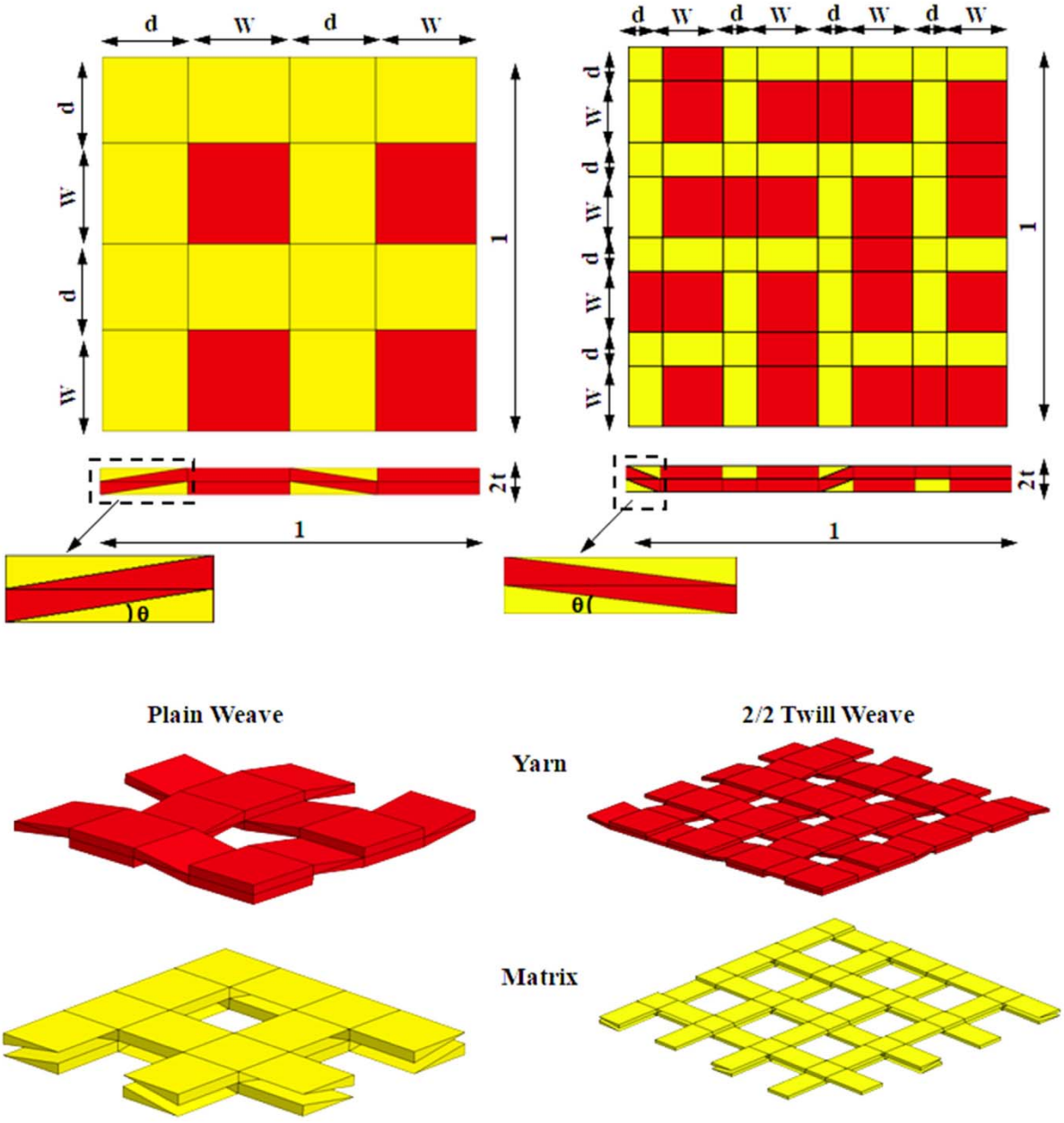

Fig. 7. Unit cells for plain and 2/2 twill weave fabric configurations used in the FSA.

We note that the actual complex microstructure geometry is approximated here by using wedge and cuboidal sub-volumes. As the response of a composite is sensitive to its microstructure one can expect an FEA to better predict properties of the unit cell. We note that the FEA was used in [52] to homogenize thermo-mechanical properties of a tungsten heavy alloy that is composed of tungsten particulates immersed in iron-nickel matrix. The concentration tensors for unidirectional piezoelectric and shape memory alloy fibers embedded in a matrix are given in [53].

It is difficult to quantify errors introduced by assuming periodicity of the microstructure needed in the FSA. However, by studying numerous microstructures of different periodicity, one can use a statistical method to homogenize properties of an actual microstructure; this has not been pursued here.

3.4. Prediction of strengths of woven fabric composite

Fig. 9 shows the stress–strain curve for unidirectional loading in tension and compression both along and transverse to the fiber direction for E-glass/epoxy composite with $V_f = 0.75$ whose strength properties are listed in Table 5. The curves have been plotted by taking H = 2, -3, and 0, respectively, for hardening, softening and perfectly plastic responses in post-failure (or post - yielding) deformations.

The strength properties of the yarn and the resin used in the analysis of plain and twill weave are listed in Table 5, and the geometric and the material properties for the weaves are given in Tables 4a and 4b. The failure analysis was carried out for four different weaves of E-glass fiber-reinforced composites listed in Table 6. The softening/hardening parameter for the yarn and the resin was taken to be -3 and -250 MPa, respectively. We found that H < -250 MPa resulted in numerical issues

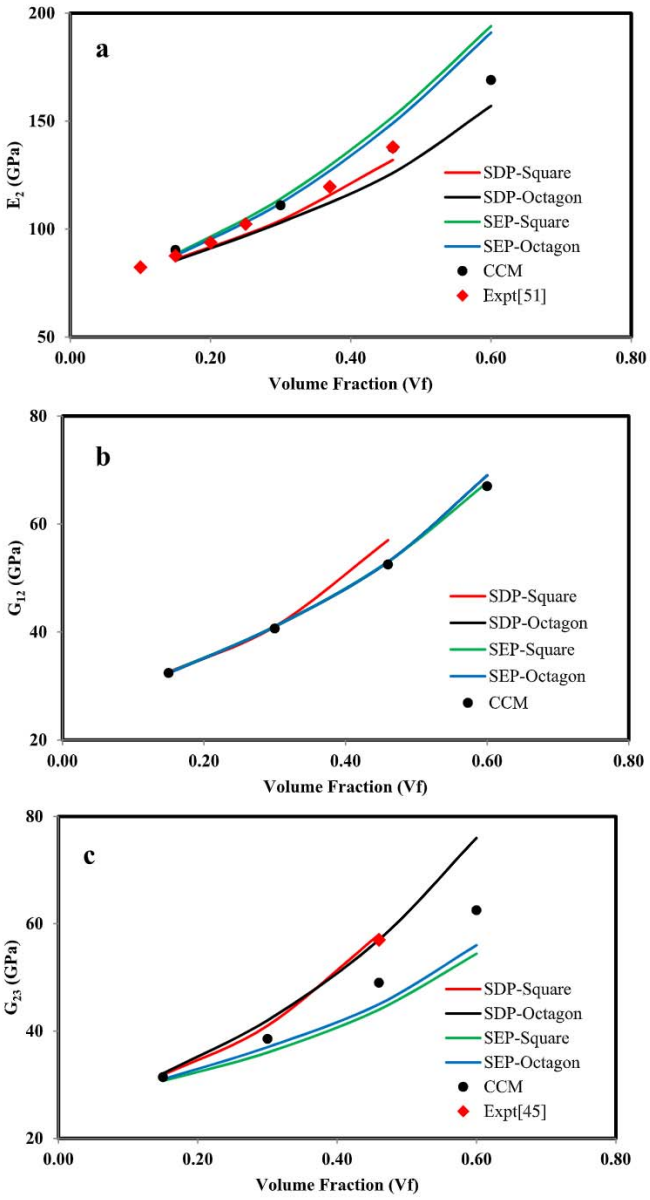

Fig. 8. a–e: For different volume fraction of the fibers, elastic constants predicted from the FSA approach (for SDP and SEP configurations having square and octagonal fibers) and the concentric cylinder model.

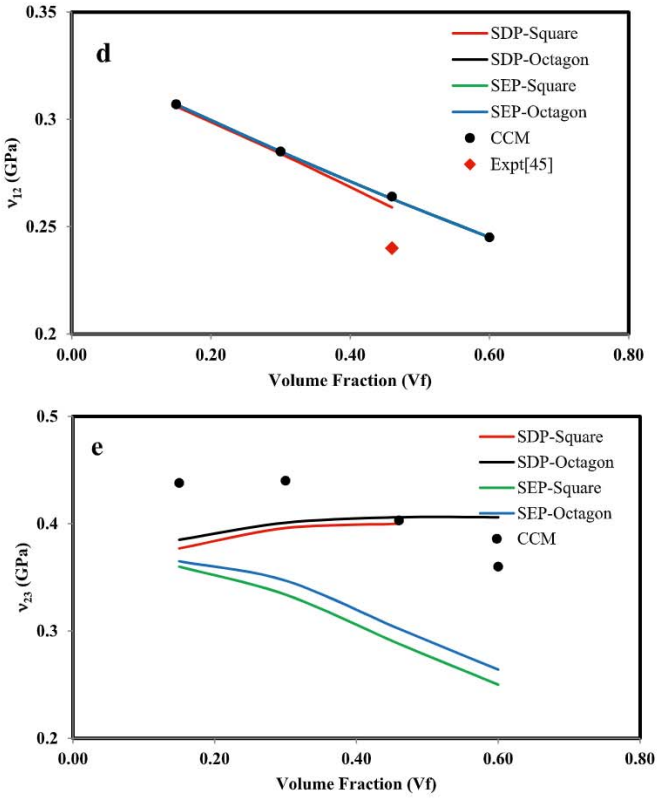

Fig. 8. (*continued*).

Table 5
Strength properties of the yarn and the resin used in the FSA analysis.

	V_f	F_{1t} (MPa)	F_{1c} (MPa)	F_{2t} (MPa)	F_{2c} (MPa)	F_4 (MPa)	F_6 (MPa)
E-glass/epoxy [23]	0.75	1551	721	46	141	85	85
E-glass/epoxy [54,55]	0.65	1140	620	50	147	61	61
E-glass/vinylester [23]	0.80	1655	769	50	150	89	89

	Y_{matrix} (MPa)
Epoxy [23]	70
Vinylester [23]	73

Table 6
Weaves used in the study.

	Weave	Material	V_f/V_y	V_f/V_c
1 [56]	Plain	E-Glass/Vinylester	0.8	0.5
2 [57]	Plain	E-Glass/Epoxy	0.65	0.35
3 [23]	Twill	E-Glass/Epoxy	0.75	0.38
4 [23]	Twill	E-Glass/PE/Epoxy Hybrid	0.75/0.75	0.52

in the FSA approach. Fig. 10a and b compares the predicted response of plain and twill weave fabrics, respectively, with those reported in the literature. It is seen that the present approach not only captures the nonlinearity in the stress–strain curve associated with the matrix damage but it also predicts well the ultimate failure of the weave due to the fiber failure in the yarns along the loading direction.

Reasons for differences between predicted and experimental peak load/stress for woven fabrics include simplification of the micro-structure to accommodate the FSA approach, and the assumption of the linearly elastic behavior prior to damage initiation in the failure model that neglects nonlinearities observed in experiments.

3.5. Limitation of the FSA approach

Complex micro-structures have been approximated by the periodic ones, and sizing of fibers used to enhance their bonding to the matrix has been neglected. Fiber cross-sections have been assumed to be uniform, which rarely occurs. Also, significant computational resources are needed to generate concentration tensors that require considering up to a million points in the frequency domain for each sub-cell in a unit cell.

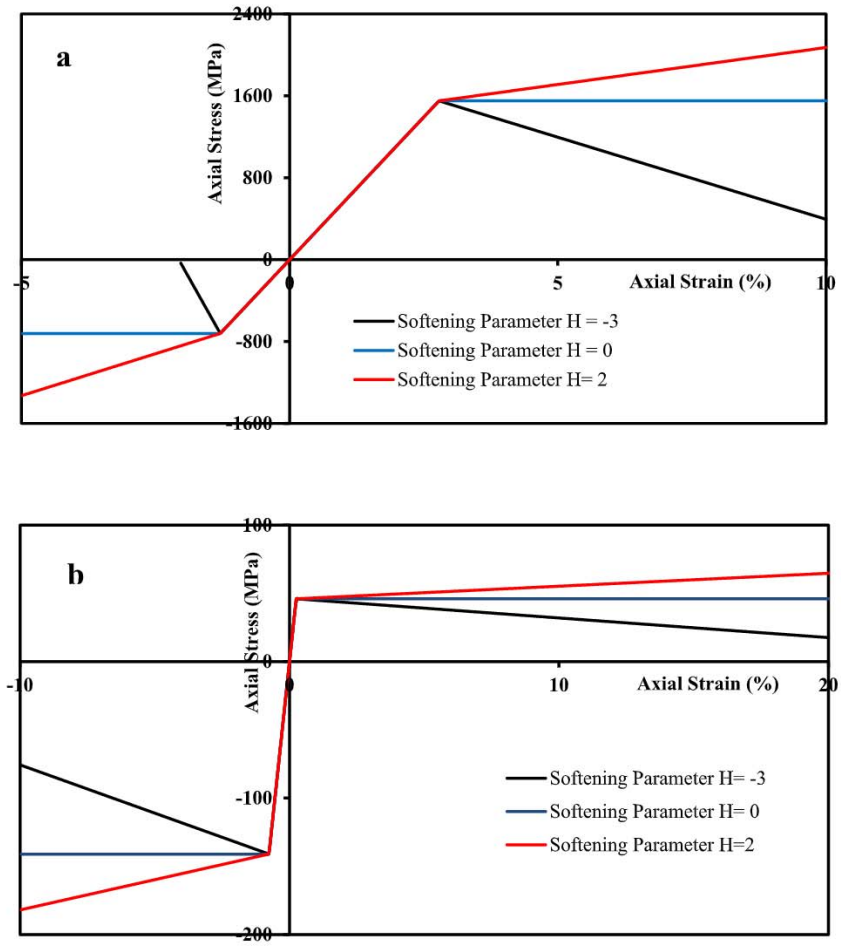

Fig. 9. Stress–strain response of unidirectional fiber-reinforced composite showing linear hardening/softening during post-failure deformations for loading (a) along, and (b) transverse to the fibers.

4. Conclusions

The introduction of a wedge along with cuboidal sub-volumes has allowed us to employ the Fourier Series Analysis (FSA) approach for analyzing complex micro-structures. We have deduced effective properties of (i) unidirectional fiber-reinforced composites with fibers of different cross-sections with square edge, square diagonal and hexagonal close packing arrangements (SEP, SDP and HCP), as well as of (ii) both plain and twill weave woven yarn reinforced composites. It is found that the transverse elastic modulus and the shear moduli are sensitive to changes in the unit cell configuration and the fiber shape. The SEP (SDP) arrangement with square (circular) fibers gives the highest (least) values of elastic constants and the ultimate strength. Elastic constants for weaves predicted from the FSA are close to those reported in the literature that were predicted either by different methods or from the test data.

The analysis of elastic–plastic deformations showed that the SEP configuration with square cross-section fibers has the stiffest response while the SDP configuration with octagonal fibers has the softest and the star shaped fibers falling between the two. These results are qualitatively similar to the effective response computed by other investigators using the finite element method (FEM).

Predicted elastic constants for weaves from the FSA agree well with those from other methods reported in the literature. A linear softening model based on the plasticity approach for post-failure initiation in yarn and resin captures well the nonlinear response of the composite and provides reasonable values of the ultimate strengths.

With the introduction of wedge sub-cells, a wide class/range of composites from unidirectional fiber-reinforced composites with complex fiber cross-sections to woven fabric composites can be analyzed with the FSA to not only predict elastic constants but also to analyze inelastic deformations and failure. Since the approach is semi-analytical it is computationally less intensive than numerical homogenizing approaches.

Future work could include accounting for strain-rate and temperature dependence of moduli of the constituents, and delineating their effects on the response of the composite.

Declaration of competing interest

The authors declare that they have no known competing financial interests or personal relationships that could have appeared to influence the work reported in this paper.

Acknowledgments

RCB's work was partially funded by the Office of Naval Research grant N00014-18-1-2548 to Virginia Polytechnic Institute and State University with Dr. Y. D. S. Rajapakse as the Program Manager. Gopinath would like to acknowledge the encouragement from his manager and colleagues.

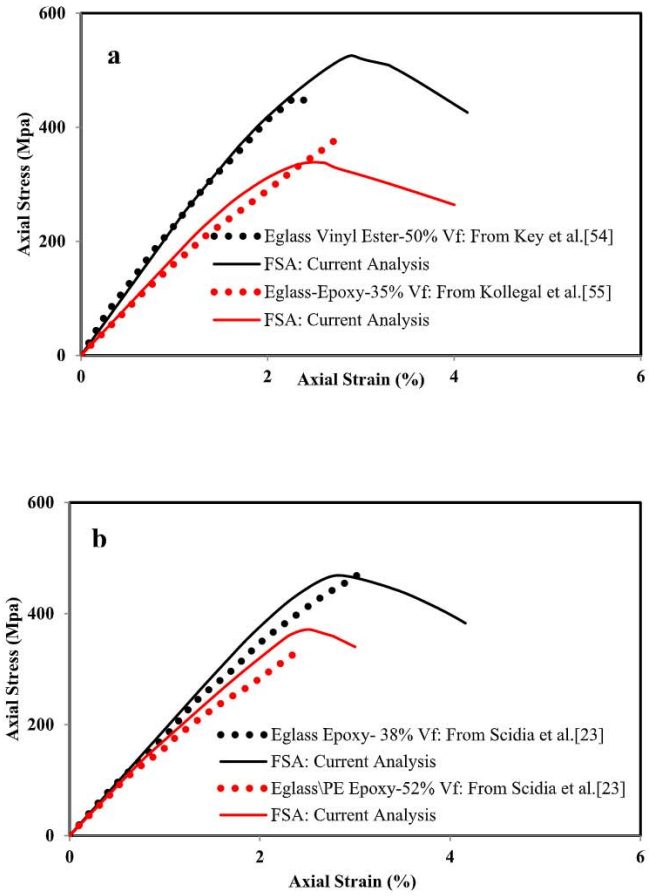

Fig. 10. Stress–strain response of E-glass woven fiber-reinforced composite till failure for (a) plain, and (b) twill weave.

References

[1] T. Mori, K. Tanaka, Average stress in matrix and average elastic energy of materials with mis-fitting inclusions, Acta Metall. 21 (1973) 571–574.

[2] Y. Benveniste, A new approach to the application of the Mori–Tanaka's theory in composite materials, Mech. Mater. 6 (1987) 147–157.

[3] J. Aboudi, Micromechanical analysis of composites by the method of cells, Appl. Mech. Rev. 42 (7) (1989) 193–221.

[4] M. Paley, J. Aboudi, Mech. Mater. 14 (1992) (1989) 127–139.

[5] S. Nemat-Nasser, M. Taya, On effective moduli of an elastic body containing periodically distributed voids, Quart. Appl. Math. 39 (1981) 43–59.

[6] S. Nemat-Nasser, T. Iwakuma, M. Hejazi, On composites with periodic structure, Mech. Mater. 1 (1982) 239–267.

[7] J. Ye, X. Chen, Z. Zhai, B. Li, Y. Duan, Z. He, Predicting the elasto-plastic response of fiber reinforced metal matrix composites, Mech. Compos. Mater. 46 (4) (2010).

[8] M.J. Pindera, B.A. Bednarcyk, An Efficient Implementation of the GMC Micromechanics Model for Multi-Phased Materials with Complex Microstructures. NASA Contractor Report 202350, 1997.

[9] B.A. Bednarcyk, S. Arnold, Micromechanics-based modeling of woven polymer matrix composites, AIAA J. 41 (9) (2003) 1788–1796.

[10] B. Bednarcyk, M.J. Pindera, Micromechanical Modeling of Woven Metal Matrix Composites. NASA Contractor Report 204153, 1997.

[11] G. Wang, S. Li, H.-N. Nguyen, N. Sitar, Effective elastic stiffness for periodic masonry structures via eigen strain homogenization, J. Mater. Civ. Eng. 19 (3) (2007) 269–277.

[12] K.P. Walker, A.D. Freed, E.H. Jordan, Micro-stress analysis of periodic composites, Compos. Eng. 1 (1) (1991) 29–40.

[13] G. Gopinath, R.C. Batra, A comparative analysis of analytical micromechanics based approaches to study elasto-plastic behavior of heterogeneous material, Int. J. Mech. Sci. 148 (2018) 540–553.

[14] G. Gopinath, R.C. Batra, Sensitivity of responses of three micro-mechanics approaches to change in unit cell configuration and inclusion shape, Compos. Struct. 213 (2019) 118–132.

[15] G.P. Tandon, R.L. Weng, A theory of particle reinforced plasticity, J. Appl. Mech. 55 (1988) 126–135.

[16] D.C. Lagoudas, A.C. Gavazzi, H. Nigam, Elastoplastic behavior of metal matrix composites based on incremental plasticity and the Mori–Tanaka averaging scheme, Comput. Mech. 8 (1991) 192–203.

[17] M. Paley, J. Aboudi, Micromechanical analysis of composites by the generalized cells model, Mech. Mater. 14 (1992) 127–139.

[18] E. Pruchnicki, Homogenized nonlinear constitutive law using fourier series expansion, Int. J. Solids Struct. 35 (16) (1998) 1895–1913.

[19] Kevin P. Walker, Alan D. Freed, Eric H. Jordan, Thermo-viscoplastic analysis of fibrous periodic composites by the use of triangular sub-volumes, Compos. Sci. Technol. 501 (1) (1994) 71–84.

[20] T. Ishikawa, T.W. Chou, Elastic behavior of woven hybrid composites, J. Compos. Mater. 16 (1982) 2–19.

[21] T. Ishikawa, T.W. Chou, One dimensional micromechanical analysis of woven fabric composites, AIAA J. 21 (12) (1983) 1714–1721.

[22] N.K. Naik, V.K. Ganesh, An analytical method for plain weave fabric composites, Composites 26 (4) (1995) 281–289.

[23] D. Scida, Z. Abouraa, M.L. Benzeggagh, E. Bocherens, A micromechanics model for 3D elasticity and failure of woven-fiber composite materials, Compos. Sci. Technol. 59 (1999) 505–517.

[24] E.J. Barbero, J. Trovillion, J.A. Mayugo, K.K. Sikkil, Finite element modeling of plain weave fabrics from photomicrograph measurements, Compos. Struct. 73 (1) (2006) 41–52.

[25] D. Blackketter, D. Walrath, A. Hansen, Modeling damage in a plain weave fabric-reinforced composite material, J. Compos. Technol. Res. 15 (2) (1993) 136–142.

[26] J.D. Whitcomb, Three Dimensional Stress Analysis of Plain Weave Composites, NASA Technical Memorandum 101672, 1989.

[27] Sun-Pui Ng, Ping-Cheung Tse, Kwok-Jing Lau, Numerical and experimental determination of in-plane elastic properties of 2/2 twill weave fabric composites, Composites B 29 (1998) 735–744.

[28] P.H. Wen, M.H. Aliabdi, Mesh-free micromechanical model for woven fabric composite elastic moduli, J. Multiscale Model. 1 (2) (2009) 303–319.

[29] L.Y. Li, P.H. Wen, M.H. Aliabadi, Meshfree modeling and homogenization of 3D orthogonal woven composites, Compos. Sci. Technol. 71 (15) (2011) 1777–1788.

[30] A. Tabiei, Y. Jiang, Woven fabric composite material model with material non-linearity for nonlinear finite element simulation, Int. J. Solids Struct. 36 (1999) 2757–2771.

[31] R. Tanov, A. Tabiei, Computationally efficient micromechanical models for woven fabric composite elastic moduli, J. Appl. Mech. 68 (2001) 553–560.

[32] G.J. Dvorak, Micromechanics of inelastic composite materials: Theory and experiment, J. Eng. Mater. Technol. 115 (1993) 327–338.

[33] I. Lapczy, J.A. Hurtado, Progressive damage modeling in fiber-reinforced materials, Composites A 38 (11) (2007) 2333–2341.

[34] F.P. Van Der Meer, L.J. Sluys, Continuum models for the analysis of progressive failure in composite laminates, J. Compos. Mater. 43 (20) (2009) 2131–2154.

[35] A.E.A. El-Sisi, H.M. El-Emam, H.A. Salim, H.E.M. Sallam, Efficient 3D modeling of damage in composite materials, J. Compos. Mater. 49 (7) (2015) 817–828.

[36] C.T. Sun, J.L. Chen, A simple flow rule for characterizing nonlinear behavior of fiber composites, J. Compos. Mater. 23 (1989) 1009–1020.

[37] S. Ogihara, K.L. Reifsnider, Characterization of nonlinear behavior in woven composite laminates, Appl. Compos. Mater. 9 (2002) 249–263.

[38] J. Cho, J. Fenner, B. Werner, I.M. Daniel, A constitutive model for fiber-reinforced polymer composites, J. Compos. Mater. 44 (26) (2010) 3133–3150.

[39] D.R. Hufner, Constitutive theories for woven composite structures subjected to shock loading; experimental validation using a conical shock tube, Shock Vib. 19 (2012) 123–144.

[40] F.P. Van Der Meer, L.J. Sluys, Interaction between intra-ply and inter-ply failure in laminates, in: P.P. Camanho, C.G. Dávila, S.T. Pinho, J.J.C. Remmers (Eds.), Mechanical Response of Composites, 2008, pp. 141–160 (Chapter 7).

[41] J.C. Simo, T.J.R. Hughes, Computational Inelasticity, Springer-Verlag, New York, 1998.

[42] J.R. Brockenbrough, S. Suresh, Plastic deformation of continuous fiber-reinforced metal-matrix composites: Effects of fiber shape and distribution, Scr. Metall. Mater. 24 (2) (1990) 325–330.

[43] M.V. Pathan, V.L. Tagarielli, S. Patsias, Effect of fiber shape and inter-phase on the anisotropic visco-elastic response of fiber composites, Compos. Struct. 162 (2017) 156–163.

[44] F. Agnese, F. Scarpa, Macro-composites with star-shaped inclusions for vibration damping in wind turbine blades, Compos. Struct. 108 (2014) 978–986.

[45] A. Paknia, A. Pramanik, A.R. Dixit, S. Chattopadhyaya, Effect of size, content and shape of reinforcements on the behaviour of metal matrix composites (MMCs) under tension, J. Mater. Eng. Perform. 25 (2016) 4444–4459.

[46] J.R. Brockenbrough, S. Suresh, H.A. Wienecke, Deformation of metal-matrix composites with continuous fibers: geometrical effects of fiber distribution and shape, Acta Metall. Mater. 39 (5) (1991) 35–752.

[47] M. Herráez, C. González, C.S. Lopes, R. Guzmán de Villoria, J. Lorca, T. Varela, J. Sánchez, Computational micromechanics evaluation of the effect of fiber shape on the transverse strength of unidirectional composites: an approach to virtual materials design, Composites A 91 (2) (2016) 484–492.

[48] L. Yang, X. Liu, Z. Wua, R. Wang, Effects of triangle-shape fiber on the transverse mechanical properties of unidirectional carbon fiber reinforced plastics, Compos. Struct. 152 (2016) 617–625.
[49] L. Yang, Z. Li, T. Sun, Z. Wu, Effects of gear-shape fibre on the transverse mechanical properties of unidirectional composites: Virtual material design by computational micromechanics, Appl. Compos. Mater. 24 (2017) 1165–1178.
[50] P. Chaphalkar, A. Kelkar, Analytical and experimental elastic behavior of twill woven laminate, in: Proceedings of the 12th International Conference on Composite Materials, Paris, France, July 1999.
[51] C.C. Chamis, Characterization and design mechanics for fiber reinforced metals. NASA TN d-5784, 1970.
[52] B.M. Love, R.C. Batra, Determination of effective thermomechanical parameters of a mixture of two thermoviscoplastic constituents, Int. J. Plasticity 22 (2006) 1026–1061.
[53] B. Jiang, R.C. Batra, Micromechanical modeling of a composite containing piezoelectric and shape memory alloy inclusions, J. Intelligent Mater. Syst. 12 (2001) 165–182.
[54] J. Aboudi, Micro-failure prediction of the strength of composite materials under combined loading, J. Reinf. Plast. Compos. 10 (1991) 495–503.
[55] T.E. Tay, G. Liu, V.B.C. Tan, X.S. Sun, D.C. Pham, Progressive failure analysis of composites, J. Compos. Mater. 42 (18) (2008) 1921–1966.
[56] C.T. Key, S.C. Schumacher, A.C. Hansen, Progressive failure modeling of woven fabric composite materials using multi-continuum theory, Composites B 38 (2007) 247–257.
[57] M. Kollegal, S.N. Chatterjee, G. Flanagan, Progressive failure analysis of plain weaves using damage mechanics based constitutive laws, Int. J. Damage Mech. 10 (4) (2001) 301–323.